Geochimica et Cosmochimica Acta 361 (2023) 24–39

Contents lists available at ScienceDirect

Geochimica et Cosmochimica Acta

journal homepage: www.elsevier.com/locate/gca

Molecular-scale insight into selenium isotope fractionation caused by adsorption on Fe (oxyhydr)oxides

Hai-Bo Qin [a,*], Jian-Ming Zhu [b], Hong-Tao He [c], Lei Fang [d,e], Wenpo Xu [a], Decan Tan [a], Zexing Cao [e], Masato Tanaka [f], Yoshio Takahashi [f]

[a] State Key Laboratory of Environmental Geochemistry, Institute of Geochemistry, Chinese Academy of Sciences, Guiyang 550081, China
[b] State Key Laboratory of Geological Processes and Mineral Resources, China University of Geosciences, Beijing 100083, China
[c] Collaborative Innovation Center of Resource Exploration and Exploitation, Hebei University of Engineering, Handan 056038, China
[d] College of Materials Science and Engineering, Huaqiao University, Xiamen, 361021, China
[e] State Key Laboratory of Physical Chemistry of Solid Surfaces and Fujian Provincial Key Laboratory of Theoretical and Computational Chemistry, College of Chemistry and Chemical Engineering, Xiamen University, Xiamen 361005, China
[f] Department of Earth and Planetary Science, Graduate School of Science, The University of Tokyo, Hongo 7-3-1, Bunkyo-ku, Tokyo 113-0033, Japan

ARTICLE INFO

Associate editor: Jeffrey G. Catalano

Keywords:
Selenium isotope fractionation
Adsorption
Iron oxides: EXAFS
Density functional theory (DFT) calculations
Molecular-scale mechanism

ABSTRACT

Selenium (Se) isotopes have recently emerged as a potential proxy for tracing biogeochemical processes and reconstructing the evolution of global Se cycle in the oceans. However, little is known about Se isotope fractionation mechanism during the sequestration of dissolved Se oxyanions by marine ferromanganese oxides that are mainly composed of Fe and Mn (oxyhydr)oxides. Here we elucidate the molecular mechanism governing equilibrium Se isotope fractionation during adsorption on 2-line ferrihydrite, by combining isotope ratio measurements, extended X-ray absorption fine structure (EXAFS) analyses, and high level quantum chemical calculations. Results show that Se isotopes can be fractionated 0.89‰ ($\Delta^{82/76}Se_{aqueous\text{-}adsorbed}$) with enrichment of lighter isotopes in the solid phase during the adsorption of Se(IV) on 2-line ferrihydrite, which is primarily driven by the formation of bidentate-binuclear inner-sphere complexes. By contrast, little or no Se isotope fractionation (<0.2‰) was observed during Se(VI) adsorption due to the outer-sphere complexation. In combination with previous results, our findings would provide molecular-scale insights into Se isotope compositions in marine ferromanganese oxides and lead to an improved understanding of Se biogeochemical cycle in the ocean. Our study also has an implication for the systematical understanding of mechanisms governing isotope fractionations of other metal oxyanions like Mo, which highlights the controls of their proton dissociation constants, electronic configurations, and radius ratios. This would improve our understanding for isotope signatures of metals in the dissolved species and the adsorbed sinks in modern and ancient environments.

1. Introduction

Selenium (Se) is of great environmental and biological interest as an essential trace element for human beings (Rayman, 2008; Lenz and Lens, 2009). Nonetheless, Se becomes toxic at high concentrations, excessive Se intake (>400 μg/d) would induce the occurrence of human Se poisoning in seleniferous areas (Yang et al., 1983; Lenz and Lens, 2009; Qin et al., 2013). Considerable efforts have been focused on the environmental geochemistry of Se to clarify the distribution, speciation, bioavailability, mobility, and fate of Se in the terrestrial environment (e.g., Catalano et al., 2006; Rayman, 2008; Zhu et al., 2008; Qin et al., 2012, 2013, 2017a,b; Schilling et al., 2015).

Selenium has six stable isotopes (^{74}Se, ^{76}Se, ^{77}Se, ^{78}Se, ^{80}Se, and ^{82}Se) and its isotope systematics is complex, because it is a redox-sensitive element with multiple oxidation states (−II, 0, IV, and VI). Selenium isotopes have recently emerged as a potential proxy for tracing biogeochemical processes and reconstructing the evolution of global Se cycle in modern and ancient environments (Johnson et al., 1999, 2000; Mitchell et al., 2012, 2016; Zhu et al., 2014; Pogge von Strandmann et al., 2015; Schilling et al., 2015; Stüeken et al., 2015; Stüeken, 2017; Kipp et al., 2017; König et al., 2019). A mechanistic understanding of Se isotope fractionation caused by different biogeochemical processes is fundamental and critical for the application of Se isotope proxy.

Selenium isotope fractionation can be induced by various

* Corresponding author.
E-mail address: qinhaibo@vip.gyig.ac.cn (H.-B. Qin).

https://doi.org/10.1016/j.gca.2023.09.009
Received 14 November 2022; Accepted 11 September 2023
Available online 15 September 2023

biogeochemical processes involving abiotic/biotic redox, adsorption, equilibrium isotope exchange, assimilation and methylation (e.g., Johnson and Bullen, 2004; Stüeken, 2017). The abiotic and/or biotic reduction of Se(VI) to Se(IV) and Se(IV) to Se(0) can impart a large Se fractionation (Johnson et al., 1999; Herbel et al., 2000; Johnson and Bullen, 2003; Schilling et al., 2020). Recent studies showed that a large fractionation can be also caused by Se oxidation (Wasserman et al., 2021; Dwivedi et al., 2022). By contrast, almost no fractionation is observed for isotope equilibrium exchange reaction between aqueous Se (IV) and Se(VI) (Tan et al., 2020). As for adsorption process, Se isotope fractionation is generally <1‰ (Johnson et al., 1999; Mitchell et al., 2013; Xu et al., 2020, 2021). However, little is known about the molecular- and atomic-scale mechanisms driving Se isotope fractionation during adsorption onto mineral surfaces.

In the modern seawater, Se dominantly occurs as dissolved Se(IV) and Se(VI) species, both of them exhibit a typical nutrient behavior with depletion in the photic zone and constant concentrations at depth (Cutter and Cutter 2001; Stüeken, 2017; Chang et al., 2017). Se abundance in seawater is very low, with 0.02–1.03 nM for Se(IV) and 0.13–1.48 nM for Se(VI) in the Eastern Tropical North Pacific Ocean (Cutter and Bruland, 1984). Interestingly, a substantial amount of Se oxyanions in seawater could be scavenged by marine ferromanganese crusts and nodules, in which Se content is generally high (>0.5 mg/kg; Takematsu et al., 1990; Rouxel et al., 2002; Koschinsky and Hein, 2003; Hein and Koschinsky, 2014; Kashiwabara et al., 2014; Stüeken, 2017). Stüeken (2017) suggested that the adsorption of Se(IV) onto ferromanganese oxides (48%) is the major Se sink in the modern ocean, followed by the partial oxyanion reduction and minor organic preservation in suboxic regions of the open ocean (45%), organic deposition and nearly quantitative oxyanion reduction in restricted euxinic basins (7%). Accordingly, it could be expected that Se isotope fractionation occurring between seawater and ferromanganese oxides has a profound influence on the isotopic composition of Se in global modern seawater, as reported previously for other elements like Mo (Barling and Anbar, 2004; Goldberg et al., 2009).

Iron (oxyhydr)oxides have a great affinity for Se oxyanions and act as the important sink of Se in environments (Balistrieri and Chao, 1990; Catalano et al., 2006; Harada and Takahashi, 2008; Qin et al., 2017a; Stüeken, 2017). Mitchell et al. (2013) preliminarily reported Se isotope fractionation behavior during adsorption on different Fe oxides ($\Delta^{82/76}Se_{aqueous\text{-}adsorbed} < 1‰$, with a mean of 0.2‰), but the equilibrium Se isotope fractionation caused by adsorption is not assessed in detail because aqueous Se has been fully removed within a short time (<1 h). In fact, numerous studies have observed distinct isotope fractionation behavior at different adsorption stages (particularly at the initial stage) for many elements (such as Tl, Zn, and Ca) (Nielsen et al., 2013; Dong and Wasylenki, 2016; Brazier et al., 2019). Recently, Xu et al. (2020) investigated equilibrium Se isotope fractionation during the adsorption of Se oxyanions on metal oxides for up to 96 h, showing that lighter isotopes prefer to distribute to the mineral, with the fractionation of 0.87‰ for crystalline hematite at pH 5. However, the dominant Fe component in marine ferromanganese oxides is ferrihydrite (Hein and Koschinsky, 2014; Yang et al., 2018; Qin et al., 2019), equilibrium Se isotope fractionation at this mineral–water interface is largely unclear, and the effect of such adsorption on the isotopic compositions of seawater and ferromanganese sediments is still unknown. Thus, it is critical to examine equilibrium Se isotope fractionation during the immobilization by ferrihydrite and clarify the molecular mechanism for improving our understanding on the global Se cycling.

To move beyond phenomenological exploration of different isotope effects for some heavy elements (e.g., Cu, Zn, Ni, Mo, and W) during adsorption, a number of studies have been performed to explore molecular-scale mechanisms by first-principles density functional theory (DFT) calculations and extended X-ray absorption fine structure (EXAFS) analyses (Juillot et al., 2008; Li and Liu, 2010; Kashiwabara et al., 2011, 2017; Wasylenki et al., 2011; Gou et al., 2018; Gueguen et al., 2018). It has been suggested that isotopic fractionations of elements caused by adsorption onto minerals are mainly driven by the symmetry change in the adsorbed species (Kashiwabara et al., 2011, 2017; Gou et al., 2018; Tanaka et al., 2018). However, so far, the correlation between Se isotope fractionation and coordination environments of adsorbed Se complexes on Fe (oxyhydr)oxides is still not demonstrated, and the equilibrium fractionation factor has not been estimated theoretically.

In the present study, we provided the assessment of the direction and magnitude of equilibrium Se isotope fractionation during adsorption on 2-line ferrihydrite. Combining EXAFS analyses and high level quantum chemical calculations with Se isotope measurements, we explored the molecular-scale mechanism responsible for Se isotope fractionation caused by adsorption process at the mineral–water interface of Fe (oxyhydr)oxides. Furthermore, we proposed a general mechanism driving isotopic fractionations of metal oxyanions that highlights the change in local structures of the surface complexes at the molecular and atomic levels, which may help understand their isotope signatures and biogeochemical cycling in ancient and modern environments.

2. Experimental

2.1. Materials

The 2-line ferrihydrite was prepared following the procedures proposed by Schwertmann and Cornell (2000). Briefly, $Fe(NO_3)_3{\cdot}9H_2O$ (ACS reagent) was dissolved in Milli-Q water and then the pH was adjusted to ~8.0 through the dropwise addition of 5.0 M KOH solution. After aging overnight, the suspension was filtered using a 0.22 μm polyethersulfone membrane filter and rinsed thoroughly with Milli-Q water. The obtained solid phase was freeze dried and collected for adsorption experiments. The synthetic 2-line ferrihydrite was identified by X-ray diffraction (XRD), with the presence of two very broad peaks. The Brunauer–Emmett–Teller surface area of this ferrihydrite was 330 m^2/g. No Se was detected in this 2-line ferrihydrite after acid digestion.

The Se(IV) and Se(VI) stock solutions (6330 μM) were prepared by dissolving Na_2SeO_3 and K_2SeO_4 (Alfa Aesar) in Milli-Q water (18.2 MΩ), respectively. The $\delta^{82/76}Se$ values of Se(IV) and Se(VI) stock solution were −1.18 ± 0.06‰ (n = 12, 2SD) and 1.18 ± 0.06‰ (n = 12, 2SD), respectively. The ionic strength (IS) of fluids was adjusted by NaCl (background electrolyte). All solutions were freshly prepared prior to experiments. The labwares used in the adsorption and isotopic experiments were carefully cleaned to avoid possible contamination.

2.2. Adsorption experiments

To evaluate the influence of common environmental factors on the isotope fractionation between aqueous and adsorbed Se, three types of Se adsorption experiments for 2-line ferrihydrite were carried out under ambient conditions: (i) kinetic adsorption experiments, (ii) adsorption edge experiments, and (iii) adsorption isotherm experiments.

All batch experiments were performed in 50 mL centrifuge tubes filled with 2-line ferrihydrite suspension (solid/liquid ratio = 0.1 g/L) and continuously stirred a reciprocal shaker at 120 rpm and room temperature. The kinetic adsorption experiment (time-series) was performed at pH 7 and 0.01 M NaCl over a time period of 96 h. The initial concentration of Se(IV) and Se(VI) was set at 38.8 μM.

For the adsorption edge experiments (pH-dependent), suspensions were equilibrated at different pH (4, 5, 6, 7, and 8) with a constant starting Se(IV) concentration of 38.8 μM. These pH conditions were selected because (i) they cover the pH ranges in natural system (e.g., seawater: 7.5–8.4, soil: 5–8) (Halevy and Bachan, 2017); and (ii) the predominant Se(IV, $HSeO_3^-$) and Se(VI, SeO_4^{2-}) species do not change significantly across the pH range 4–8 based on the calculation by Visual MINTEQ.3.1 (Gustafsson, 2018; Fig. S1). The applications of 0.01 M and 0.7 M NaCl (representing natural freshwater and seawater, respectively)

were intended to investigate the effect of ionic strength on adsorption. For adsorption isotherm experiments (concentration-control), suspensions were equilibrated at fixed pH 7 and 0.01 M NaCl with different Se (IV) initial concentrations (0.66–260 μM). These initial Se(IV) concentrations were selected because (i) the higher initial Se concentration would avoid the full Se removal from solution during adsorption, which allows us to determine Se isotope ratio in the liquid phase for revealing Se isotope fractionation behavior; and (ii) the concentrations of Se adsorbed on ferrihydrite (Se/Fe atomic ratio > 0.00004) cover the Se content found in marine ferromanganese oxides (e.g., Se/Fe atomic ratio ≈ 0.00007; Kashiwabara et al., 2014). While adding Se, the suspension was stirred vigorously to avoid the formation of Se precipitates due to local oversaturation. These adsorption edge and isotherm experiments were performed for 48 h, which is long enough to achieve the steady-state as supported by the kinetic experiment. It should be noted that pH-dependent and concentration-control experiments were not performed for Se(VI) due to little or no isotope fractionation during adsorption (Xu et al., 2020, 2021).

Over the course of all experiments, the pH buffers were not employed in order to minimize undesired complexation and particle aggregation. The pH was adjusted to desired values by adding < 20 μL 0.1 M NaOH or HCl solution as necessary. The solid and liquid phases were separated after individual adsorption experiments. The supernatants were filtered through a 0.22 μm polyethersulfone membrane filter, and then the filtrate was stored in a HDPE tube for analysis. While the solid phase was rinsed with MQ water to remove trace amounts of dissolved Se and then dissolved in 5 M HCl for further analysis.

2.3. Se concentration analysis

Concentration of Se was determined by hydride generation atomic fluorescence spectrometry (HG-AFS) following the method described in our previous studies (Qin et al., 2012). As for the Se(IV) adsorption experiments, Se content in the filtrate was determined directly by HG-AFS after diluting a small aliquot of filtrate with 0.75 M HCl. In the case of Se(VI), the filtrate was reduced to Se(IV) in 5 M HCl at 95–100 °C for 1 h, then the final solution was diluted for HG-AFS analysis. The relative standard deviation (RSD) for Se analysis was <5%. The Se surface coverage was calculated from the difference in concentrations between the initial and equilibrium solutions by considering the BET-N_2 surface area of 2-line ferrihydrite and the solid/liquid ratio.

2.4. Sample purification and Se isotope measurement by MC-ICP-MS

Sample purification procedures were performed according to those proposed by Xu et al. (2020). In brief, the ^{74}Se-^{77}Se double spike was added to the sample containing ~100 ng Se in a 15 mL PFA beaker, and the ratio of spike to sample ($^{77}Se_{spike}/^{78}Se_{sample}$) was close to 2 for minimizing errors during data reduction. After equilibration overnight, the PFA beaker was placed on a hot plate at 90 °C to evaporate the sample to incipient dryness. Then, 1.0 mL of 0.03 M potassium persulfate ($K_2S_2O_8$) was added into the beaker and heated at 130 °C for >2 h. The obtained sample solution was loaded onto the column containing 1.0 mL anion exchange resin (AG1-X8, 100–200 mesh), and then washed with MQ water and 0.1 M HCl. Finally, Se(VI) was recovered from the resin with 5.0 M HCl. After the Se(VI) solution was reduced to Se(IV) by heating at 95–100 °C for 1 h, the sample solution was diluted to 2.0 ± 0.1 M HCl for Se isotope measurement.

Selenium isotopes were determined using the Nu Plasma II MC-ICP-MS (Nu Instrument, UK) at the State Key Laboratory of Environmental Geochemistry, Institute of Geochemistry, Chinese Academy of Sciences. Sample solution was introduced into the plasma through a hydride generator, in which the gaseous H_2Se was produced through the reaction of sample and a mixture of 0.3% $NaBH_4$ and 0.4% NaOH solution. All of the Se isotope signals (^{74}Se, ^{76}Se, ^{77}Se, ^{78}Se, ^{80}Se, and ^{82}Se) were determined simultaneously using the Faraday cups at the low resolution mode. An iterative data reduction routine was used to correct interferences and obtain Se isotopic ratio. Details of Se isotope measurements and interference corrections are described in previous studies (Tan et al., 2020; Xu et al., 2020, 2021).

The Se isotopic composition was reported relative to NIST SRM3149 in the delta notation:

$$\delta^{82/76}Se = [(^{82/76}Se_{sample}/^{82/76}Se_{standard}) - 1] \times 1000 \quad (1)$$

where $^{82/76}Se_{sample}$ and $^{82/76}Se_{standard}$ are the $^{82/76}$Se ratio in the sample and the standard SRM 3149, respectively. During the analysis, the SRM 3149 solution was determined every 3–5 samples to monitor the stability of the instrument. The $\delta^{82/76}$Se value of SRM 3149 was 0.00 ± 0.10‰ (2SD, n = 150) during a 3-years period, whereas that of an in-house MH495 reference solution was −3.44 ± 0.11‰ (2SD, n = 45), which are highly comparable to those reported in other studies (Stüeken et al., 2013, 2015; Schilling et al., 2020; Labidi et al., 2018). Thus, the accuracy and precision of the analytical procedures for Se isotope are reliable in this study.

The Se isotopic compositions of all aqueous phases obtained by filtration were directly measured by MC-ICP-MS in this study. The Se isotopic ratios of adsorbed samples can be obtained by either direct measurement or mass balance calculation. However, the isotope signature of the solid phase during analysis might be compromised by the presence of dissolved ions (Barling and Anbar, 2004; Balistrieri et al., 2008). Although dissolved ions can be removed by water washing, it is likely that some of adsorbed species via weak electrostatic force (e.g., outer-sphere complexes) may be also removed during rinse. In the present study, Se isotope composition of the adsorbed sample was estimated by mass balance calculations to avoid possible Se loss and better compare Se isotope results from each individual experiment, considering that Se(VI) is predominantly adsorbed on minerals via weak outer-sphere complexation (Harada and Takahashi, 2008; Kikuchi et al., 2019). In fact, this method has been widely employed to investigate isotope composition and fractionation of other elements (Ge, Ga, Cu, Zn, and K) during adsorption (Pokrovsky et al., 2014; Balistrieri et al., 2008; Yuan et al., 2018; Wasylenki et al., 2020; Li et al., 2021).

Here, the $\delta^{82/76}$Se values of the adsorbed phases were calculated based on mass balance equation as follows:

$$\delta^{82/76}Se_{adsorbed} = (\delta^{82/76}Se_{stock} - \delta^{82/76}Se_{aqueous} \times (1 - f))/f \quad (2)$$

where $\delta^{82/76}Se_{stock}$, $\delta^{82/76}Se_{adsorbed}$, and $\delta^{82/76}Se_{aqueous}$ represent the $\delta^{82/76}$Se value in the stock solution, solid phase, and liquid phase, respectively; *f* and 1-*f* are the fraction of Se adsorbed and Se remaining in solution, respectively.

Furthermore, we also measured $\delta^{82/76}Se_{adsorbed}$ values in several Se (IV) adsorbed samples to check the isotope mass balance. The isotopic offset between the measured and calculated values is less than the analytical uncertainty (0.1‰). The sum of isotopic values for aqueous and measured adsorbed Se was equal to Se(IV) stock solution within the uncertainty. This suggests that $\delta^{82/76}$Se values in both liquid and solid phases reported here are highly reliable.

The equilibrium isotope fractionation caused by adsorption was calculated as the difference in the $\delta^{82/76}$Se values between aqueous and adsorbed Se, $\Delta^{82/76}Se_{aqueous\text{-}adsorbed}$ is defined as:

$$\Delta^{82/76}Se_{aqueous\text{-}adsorbed} = \delta^{82/76}Se_{aqueous} - \delta^{82/76}Se_{adsorbed} \quad (3)$$

The estimated uncertainties on the calculated $\Delta^{82/76}Se_{aqueous\text{-}adsorbed}$ stemmed from (i) the uncertainty on the fraction of Se adsorbed, and (ii) the analytical uncertainty on the isotopic composition of the initial Se solution and Se isotopic ratio of each individual experiment.

Rayleigh and Equilibrium fractionation models are used to describe Se isotopic fractionation between aqueous ($\delta^{82/76}Se_{aqueous}$) and adsorbed phases ($\delta^{82/76}Se_{adsorbed}$). The Rayleigh model considers that one phase can be continuously removed from the system, while the equilibrium model assumes continuous, reversible isotope exchange as the

reaction continues in closed systems. The two models are described based on the following equations:

Rayleigh model:

$$\delta^{82/76}Se_{aqueous} = \left(1000 + \delta^{82/76}Se_{stock}\right) \times (1-f)^{(1-\alpha_{aqueous-adsorbed})} - 1000 \quad (4)$$

Equilibrium model:

$$\delta^{82/76}Se_{aqueous} = \frac{\delta^{82/76}Se_{stock} - 1000 \times f \times (1-\alpha_{aqueous-adsorbed})}{1+f-(f \times \alpha_{aqueous-adsorbed})} \quad (5)$$

where $\alpha_{aqueous\text{-}adsorbed}$ is the fractionation factor, $\delta^{82/76}Se_{stock}$ is the measured $\delta^{82/76}$ value of initial aqueous Se(IV) (−1.18 ± 0.06‰), and f denotes the fraction of Se adsorbed on ferrihydrite (i.e., (1 − f) is the proportion of Se remaining in solution).

2.5. XAFS measurement and data analysis

The ferrihydrite adsorption experiments were run in parallel batches in order to obtain enough solid materials for X-ray absorption fine structure (XAFS) measurement. The solid phase at different reaction time (1, 5, and 24 h) was obtained by filtering the suspensions using a 0.22 μm membrane filter, and then sealed into a polyethylene bag after quick rinse with MQ water.

Selenium K-edge XAFS spectra of adsorbed samples were collected at the BL14W1 beamline of the Shanghai Synchrotron Radiation Facility (SSRF, Shanghai, China) and the 1W1B beamline of the Beijing Synchrotron Radiation Facility (BSRF, Beijing, China). The X-rays were monochromatized with a pair of Si(1 1 1) crystals and focused with a bent cylindrical mirror. The samples were placed at an angle of 45° from the incident beam to record the XAFS spectra in fluorescence mode using a Ge solid-state detector (SSD) at room temperature under ambient conditions. Energy calibration was performed using a $NaHSeO_3$ reference compound by defining the energy of 12.654 keV at the maximum peak of white line. Repeated scans were performed to improve the spectra quality, and no radiation damage was observed for the adsorbed samples during data acquisition.

The XAFS spectra were analyzed using REX2000 software (Rigaku Co. Ltd.) and FEFF 7.02 (Zabinsky et al., 1995). The background of XAFS spectra was removed by a spline smoothing method. For EXAFS analysis, the $k^3\chi(k)$ oscillation was extracted and then Fourier transformed to obtain radial structural function (RSF). The RSF was inversely transformed for spectral simulation by a curve-fitting method. Theoretical phase shifts and backscattering amplitude functions for the Se–O and Se–Fe shells were extracted from the structures of $Fe_2O(Se^{IV}O_3)_2$ and $Fe_2(Se^{VI}O_4)_3$ (Giester and Wildner, 1991; Giester, 1996). The quality of the fitting was given by the goodness of fit parameter, *R* factor, defined as:

$$R = \sum \{k^3 x_{obs}(k) - k^3 x_{cal}(k)\}^2 / \sum \{k^3 x_{obs}(k)\}^2 \quad (6)$$

where $\chi_{cal}(k)$ and $\chi_{obs}(k)$ are the calculated and experimental absorption coefficients at a given wavenumber (*k*), respectively. Details of the XAFS analysis are similar to those described in our previous studies (Qin et al., 2019, 2021).

2.6. Computational methods

2.6.1. Models

In this study, the $HSeO_3^-$ was selected as the dissolved species for Se (IV), because it is the predominant species under neutral circumstances (Fig. S1). For aqueous phase calculations, the cubic cell containing 60 water molecules and $HSeO_3^-$ were built, and then one Na atom was added in the cell to keep the charge balance. The lattice constants were set as a = b = c = 12.46 Å, so that the external pressure approaches zero kbar, and the density is approximately equal to 1 g/cm^3.

For the surface adsorption calculations, the unit cell of ferrihydrite was optimized and the lattice constants were calculated to be a = b = 5.95 Å, c = 9.32 Å, α = β = 90° and γ = 120°, which is consistent with previous studies (Pinney et al., 2009; Chappell et al., 2017). We constructed a 2 × 2 supercell (contains 112 atoms) and cleaved its (1 –1 0) and (1 0 0) faces to study the adsorption of $HSeO_3^-$ on ferrihydrite. The size of the supercell is 11.91 Å × 9.32 Å × 24.60 Å, with a vacuum layer height of approximately 15 Å. The H atoms were added to Fe atoms on the bottom to maintain charge neutrality in the surface models. The (1 –1 0) surface was chosen in this study because it is the most stable surface and one of the most commonly observed facets on ferrihydrite nanoparticles (Hiemstra, 2013). In addition, the (1 0 0) face was also chosen because it is a representative of edge termination of platy crystals of ferrihydrite, which enable the formation of surface complexes for ions (Ona-Nguema et al., 2005; Kubicki et al., 2018; Sassi et al., 2021).

In order to reduce the computational complex, the implicit solvation model was adopted implemented in VASPsol to simulate an aqueous environment (Mathew et al., 2014). The effect of solvation on the aqueous and surface species was modelled by inclusion of twelve explicit water molecules near each adsorbate. With the exception of the Fe atoms bonded to the adsorbate, the exposed Fe atoms are fully saturated with chemically adsorbed water. Note that isotope fractionation is a relatively local effect, the fractionations are closely related to the local structures of the interested atom. A solute molecule with surrounding twelve water molecules is sufficient to simulate the local structures of the Se(IV) in the solutions.

2.6.2. Computational details

All the density-functional theory (DFT) calculations were performed using VASP with the generalized gradient approximation (GGA)-Perdew-Burke-Ernzerhof (PBE) functional (Perdew et al., 1996). The DFT-D3 method was applied to treat van der Waals dispersion forces (Grimme et al., 2010). The first-principles molecular dynamics (FPMD) simulations were performed in NVT ensemble with a time step of 0.5 fs and total time of 50 ps. The temperatures were controlled by a Nosé thermostat and were set to be 298.15 K. For structural optimization, the cutoff was set to be 600 eV. The Brillouin zones were sampled with a 1 × 1 × 1 and 3 × 3 × 1 k-point grid for aqueous phase and surface adsorption calculations, and the convergence criterion of force was set to be 10^{-3} eV/Å and −0.05 eV/Å, respectively. The GGA + U method was used to treat 3d iron electrons with the Hubbard U formulation at 4 eV (Chappell et al., 2017). The magnetic moment for Fe was set referring to stable ferrimagnetic ordering for ferrihydrite (Pinney et al., 2009). The density functional perturbation theory (DFPT) implemented in PHONOPY (Togo and Tanaka, 2015) was applied to calculate phonon frequencies. While for the surface adsorption calculations, the vibrational frequencies of relevant atoms were calculated using finite differences method.

The equilibrium isotope fractionation factor (α) between the substances of A (aqueous Se solution) and B (adsorbed Se) was expressed as:

$$\alpha_{A-B} = RPFR(\mathrm{A})/RPFR(\mathrm{B}) \quad (7)$$

The reduced partition function ratio (RPFR) of each species was estimated using the following equation (Bigeleisen and Mayer, 1947; Urey, 1947):

$$\mathrm{RPFR} = \prod_i^N \frac{u_i^* \exp\left(-\frac{u_i^*}{2}\right)\left[1 - \exp\left(-u_i^*\right)\right]}{u_i \exp\left(-\frac{u_i}{2}\right)\left[1 - \exp\left(-u_i^*\right)\right]} \quad (8)$$

where u_i is related to the *i*th vibrational frequency (ν_i) with $ui = \frac{h\nu i}{kT}$; and *h, k and T* are the Planck's constant, Boltzmann constant and temperature, respectively. The temperature (*T*) was assumed to 298.15 K during calculations. N is the harmonic vibrational modes of molecules (N equals to 3n-5 for linear molecules, or 3n-6 for non-linear polyatomic molecules). The asterisk indicates the substance with heavier isotope (^{82}Se), while the one without asterisk refers to the lighter isotope (^{76}Se). The

magnitude of equilibrium isotope fractionation ($\Delta_{A\text{-}B}$) was expressed as:

$$\Delta_{A-B} = 1000 \times \ln[\alpha_{A-B}] \quad (9)$$

3. Results

3.1. Se adsorption on 2-line ferrihydrite

The results for Se adsorption on 2-line ferrihydrite are summarized in Tables 1 and S1. The adsorption was very rapid at the early stage, and then gradually increased with time and reached a constant value after 24 h for both of Se(IV) and Se(VI) species (Figs. 1A and 3A). The surface coverages of Se(IV) and Se(VI) were about 0.09 and 0.05 μmol/m^2 after 48 h reaction at pH 7, respectively. With increasing pH from 4 to 8, Se (IV) adsorption decreased gradually, with the surface coverage decreasing from 0.12 to 0.04 μmol/m^2. There was no significant difference in surface coverages between 0.01 M and 0.7 M NaCl, indicating that the ionic strength has a negligible influence on Se(IV) adsorption on 2-line ferrihydrite (Fig. 1B). This ionic strength-independent behavior likely suggests that the inner-sphere complexation is the predominant adsorption mechanism for Se(IV) on ferrihydrite at the examined pH ranges (Hayes et al., 1987). In addition, with incremental initial Se(IV) concentration ranging from 2.6 to 260 μM, the adsorption rate decreased gradually up to 32.6%, but the surface coverage increased up to 0.26 μmol/m^2 (Fig. 1C).

3.2. Se isotopic behavior during adsorption on 2-line ferrihydrite

The Se isotopic compositions of aqueous and adsorbed phases in different adsorption experiments are provided in Tables 1 and S1. In the time series experiments, the first-order observation is that the lighter Se isotope was preferentially partitioned to the solid phase, while the Se remaining in aqueous solution becomes isotopically heavier after the adsorption onto 2-line ferrihydrite. In the case of Se(IV), the Se isotopic composition in the aqueous phases ($\delta^{82/76}Se_{aqueous}$) rapidly increased from −1.20‰ and converged to a constant (~0.5‰) during the first 24 h, while the $\delta^{82/76}Se_{adsorbed}$ of the solid phases ranged from −1.73‰ to −1.5‰ (Fig. 2 and Table 1). From 24 h to 96 h, no significant change was observed for the aqueous and solid phases in the Se(IV) system. Fractionation between dissolved and sorbed Se(IV), $\Delta^{82/76}Se_{aqueous\text{-}adsorbed}$ was ~0.90‰. By contrast, the $\delta^{82/76}Se_{aqueous}$ value (1.18–1.27‰) changed insignificantly relative to Se(VI) stock solution (1.18 ± 0.06‰) throughout the Se(VI) adsorption experiment, with little or no Se isotope fractionation ($\Delta^{82/76}Se_{aqueous\text{-}adsorbed} < 0.2$‰) (Fig. 3B and Table S1). This observation indicates that the isotope equilibrium is probably achieved after ~24 h for the adsorption of both Se(IV) and Se(VI) on 2-line ferrihydrite.

In pH-dependent experiments for Se(IV), fractionation between dissolved and sorbed Se was 0.88 ± 0.11‰ at pH 7. Similar fractionation magnitude was found at pH ranging from 4 to 8, with the $\Delta^{82/76}Se_{aqueous\text{-}adsorbed}$ of 0.85–0.94‰ (Table 1). In concentration-control experiments, the Se isotopic composition of aqueous phases varied from −0.91 ± 0.10‰ to −0.31 ± 0.09‰ (Table 1). Although the isotopic compositions of dissolved Se varied widely at different initial Se(IV) concentrations, Se fractionations between the aqueous and adsorbed phases were near-identical, with $\Delta^{82/76}Se_{aqueous\text{-}adsorbed}$ ranging from 0.82 ± 0.19‰ to 0.93 ± 0.12‰ (Fig. 4 and Table 1). This can be explained by variations in adsorption percent following the same isotopic fractionation mechanism, as reported in previous studies (e.g., Li et al., 2021).

3.3. Se K-edge XAFS analyses

3.3.1. Se K-edge XANES

Fig. 5 shows the X-ray absorption near edge structure (XANES) spectra of Se-adsorbed samples prepared at different reaction times. The peak energies of the XANES spectra for Se(IV)-adsorbed materials were essentially identical to that of aqueous Se(IV) solution, irrespective of the adsorption time. Likewise, the Se(VI)-adsorbed samples also exhibited similar XANES spectra to that of Se(VI) solution. These observations clearly indicate that the oxidation state of Se does not change during the adsorption of either Se(IV) or Se(VI) on Fe (oxyhydr)oxides under our experimental conditions.

3.3.2. Se K-edge EXAFS

The $k^3\chi(k)$ spectra of Se K-edge EXAFS for Se(IV)-adsorbed materials obtained at different adsorption time were similar to each other, but disparate from that for aqueous Se(IV) solution (Fig. 6A). This difference became more obvious in their RSFs (Fig. 6B), where Se(IV)-adsorbed samples exhibited distant peaks at R + ΔR = 2.8 Å (phase shift not corrected) apart from the pronounced peaks at R + ΔR = 1.2 Å (phase shift not corrected), indicating the existence of scattering signals from Fe atoms for Se(IV)-adsorbed materials. The curve-fitting analysis showed that the second peak is assigned to the Se–Fe shell with the interatomic distance of 3.33 Å for ferrihydrite, whereas the first peak corresponds to the Se–O shell at 1.70 Å (Table 2). On the contrary, the $k^3\chi(k)$ spectra for Se(VI)-adsorbed materials prepared at different reaction time were essentially identical to that for Se(VI) solution (Fig. 7A). This implies that Se(VI) seems to be adsorbed on ferrihydrite via hydrated species, with the distance of the Se–O shell (the first prominent peak in the RSFs) at 1.65 Å (Fig. 7B and Table 2). These results are in good agreement with the structural parameters reported by previous studies (Harada and Takahashi, 2008; Kikuchi et al., 2019). Therefore, the EXAFS analyses suggest that the adsorption mechanism does not change with the reaction time. Specifically, Se(IV) is predominantly adsorbed on Fe (oxyhydr)oxides with the formation of the inner-sphere complexes, while the outer-sphere complexation is the main attachment mode for Se(VI) adsorption.

3.4. First-principles calculations of equilibrium Se isotope fractionation

To further assess the structural properties of aqueous $HSeO_3^-$, the partial radial distribution functions (PRDF) between Se and O (O atom in $HSeO_3^-$) were calculated. As shown in Fig. S2, only one peak are observed for the Se–O pair, indicating the high stability of Se–O bonding. We extracted 21 snapshots (see Fig. 8A as an illustration) from the 50 ps FPMD trajectories in every 1 ps and reoptimized their configurations. Based on those optimal configurations, we further performed phonon frequency calculations for obtaining the reduced partition function ratios ($10^3\ln\beta$) at 298.15 K. The results are presented in Fig. 8B, one can see that the calculated values of $10^3\ln\beta$ are 20.6–21.1, however, their cumulative averages in the time domains converge almost to a constant value (20.85). Our results are similar to the case of aqueous Mg^{2+} performed by Wang et al. (2019) and aqueous Br^- performed by Gao and Liu (2021).

To obtain the reduced partition function ratios (RPFR) for surface adsorption, the vibration frequencies of the atoms associated with $HSeO_3^-$ at 298.15 K need to be calculated. Before the RPFR ($10^3\ln\beta$) calculations, we preliminarily assessed the effect of the calculated region of surface models on vibration frequencies (Fig. S3). Using the optimized model, the $HSeO_3^-$ was bound to two corners of two adjacent Fe octahedrons, the average lengths of the Se–O bond were 1.76 Å and 1.74 Å (R_{Se-O}), and the average interatomic distances between Se and two Fe atoms were 3.37 Å and 3.21 Å (R_{Se-Fe}) for surface complexes at the (1 0 0) and (1 –1 0) faces of ferrihydrite, respectively (Fig. 8C). The $10^3\ln\beta$ values for surface complexes at the (1 0 0) and (1 –1 0) surfaces of ferrihydrite were calculated to be 18.87 and 21.79, respectively. The fractionation factors between aqueous $HSeO_3^-$ and the bidentate-binuclear Se complexes formed at the (1 0 0) and (1 –1 0) faces of ferrihydrite were theoretically calculated to be 1.94‰ and −0.98‰, respectively. This clearly indicates that Se(IV) isotope fractionation is dependent on the facet where the adsorption is occurring. However, it should be noted that the adsorption experiment on bulk powders of a

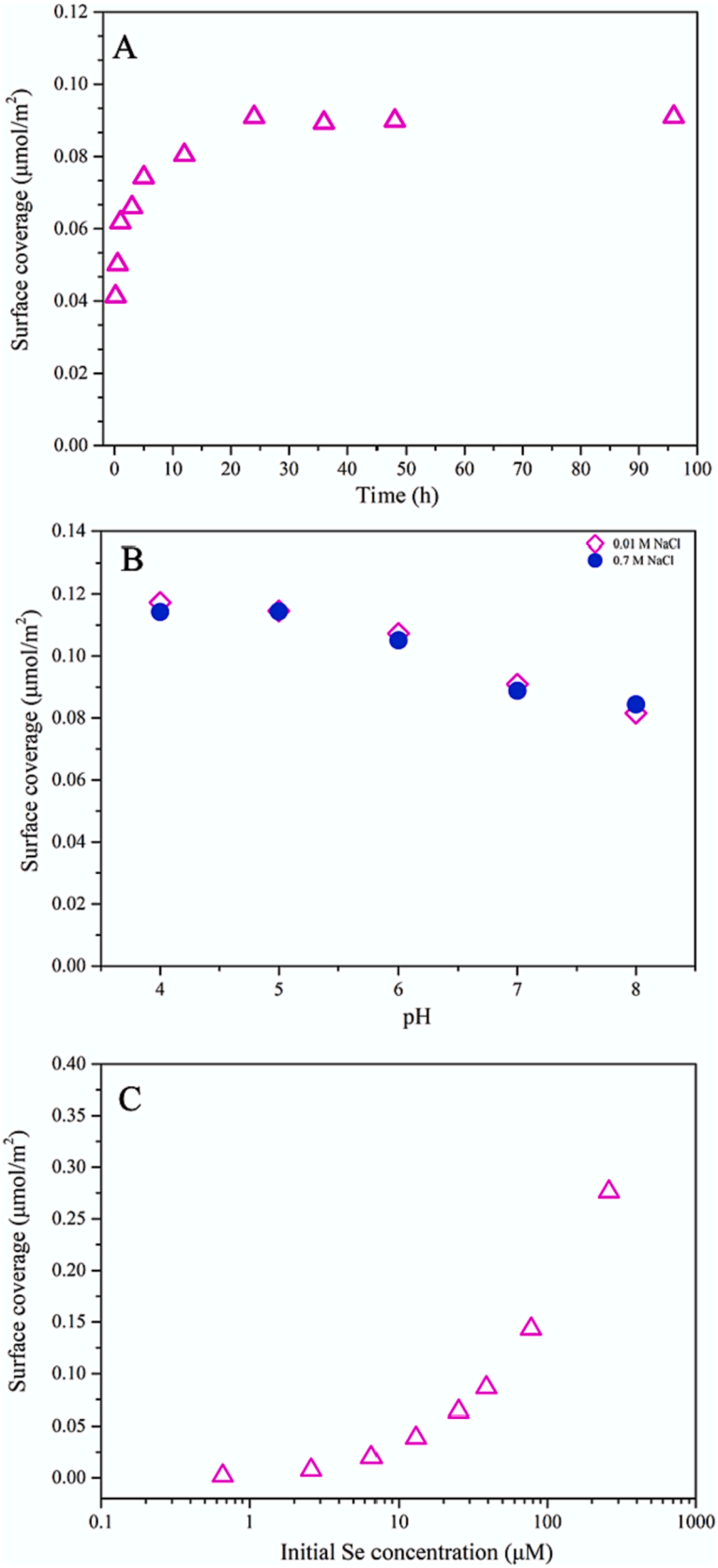

Fig. 1. Surface coverages for the adsorption of Se(IV) on ferrihydrite.

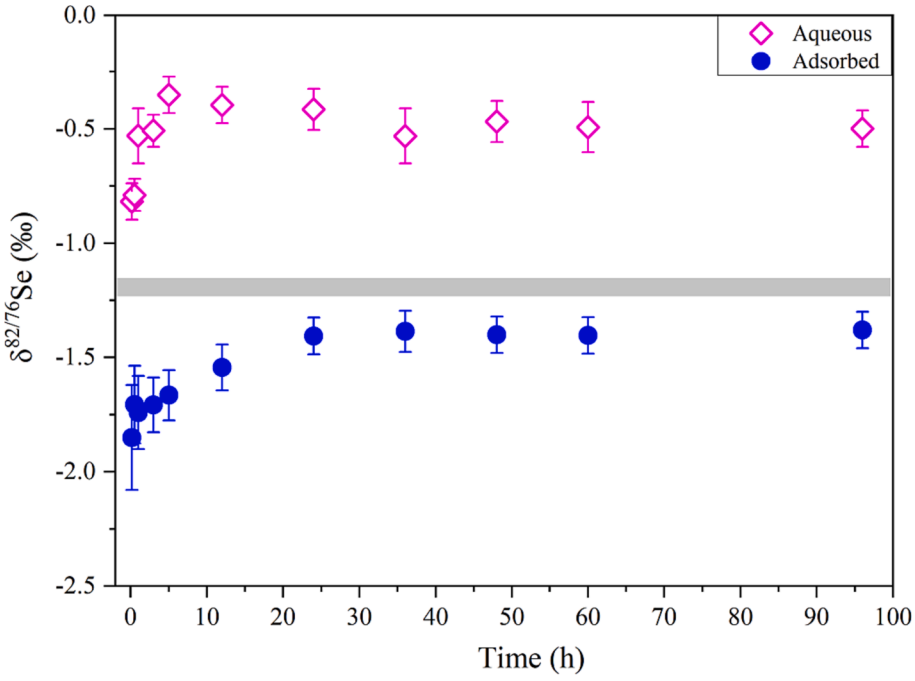

Fig. 2. The Se isotope value ($\delta^{82/76}$Se) in the liquid and adsorbed phase as a function of time for Se(IV) adsorption on ferrihydrite.

mineral probably lead to a mixture of multiple surface complexes (Kubicki et al., 2012). Similarly, we assumed that the experimental isotope fractionation is the mixture of isotope fractionations caused by Se adsorption at the (1 0 0) and (1 –1 0) faces of ferrihydrite. The contribution of (1 0 0) and (1 –1 0) faces were estimated to be ~64% and ~36%, based on the observed isotope fractionation (~0.89‰) during adsorption experiments.

4. Discussion

4.1. Se isotope fractionation caused by adsorption

Fig. 9 shows that the equilibrium fractionation model fits our experimental data better than the Rayleigh model, with the $\alpha_{aqueous\text{-}adsorbed}$ of 1.00089 ± 0.00005‰. These experimental results strongly indicate that Se isotopes are substantially fractionated during Se(IV) adsorption on 2-line ferrihydrite, likely resulting from the adequate isotopic exchange with the preferential enrichment of lighter Se isotopes in the solid phase. This equilibrium fractionation is consistent with other elements (such as Mo and W) on the mineral surfaces reported in previous studies (Barling and Anbar, 2004; Wasylenki et al., 2008, 2011, 2020; Kashiwabara et al., 2017).

In our study, we observed that the $\delta^{82/76}$Se values obtained at the initial stage (low adsorption in Fig. 10) fall on the Rayleigh fractionation line, although other $\delta^{82/76}$Se results from the kinetic experiment (duration of 96 h) appeared to follow the equilibrium fractionation. In fact, numerous studies have observed that a short-lived kinetic pattern occurs at the initial adsorption stage for elements such as Tl, Zn, and Ca (Nielsen et al., 2013; Dong and Wasylenki, 2016; Brazier et al., 2019), and then rapidly diminishes when the equilibrium is reached. Considering the similar adsorption mechanism at different reaction times revealed by our EXAFS results, one can conclude that the large fractionation at the initial stage of Se(IV) adsorption by 2-line ferrihydrite (or hematite; Xu et al., 2020) is likely govern by the kinetic effect rather than other reaction mechanisms, but an isotopic equilibrium can be eventually attained over time (after ~24 h). The observation that the initial stage of Rayleigh fractionation line and Equilibrium fractionation line seems coincident might be due to the overprint of subsequent isotope equilibrium, despite initially fast kinetic isotope fractionation. However, the Se isotope fractionation caused by kinetic effect appears to be only evident on short timescales (hours). It seems more likely that isotope fractionation caused by adsorption is close to equilibrium fractionation in nature particularly for marine environment (Little et al., 2014). This is because the residence time of Se in the ocean is thought to be 10^4 years (<26,000 years; Large et al., 2015), and the growth of ferromanganese crusts and nodules is extremely slow (1–5 mm/Ma) (Koschinsky and Hein, 2003; Hein and Koschinsky, 2014).

4.2. Molecular mechanism for Se isotope fractionation caused by adsorption

By Se K-edge XANES analyses, we clearly exclude the occurrence of Se reduction or oxidation reaction in our adsorption experiments, which is rational due to the fact that the $Fe^{2+}/Fe(OH)_3$ boundary is located at a lower Eh level than that of Se(IV)/Se(VI) shown in the Eh-pH diagram (Fig. S4, Brookins, 1988). This allows us to explore the mechanism of Se isotope fractionation caused by adsorption on Fe (oxyhydr)oxides.

4.2.1. Dominant adsorbed surface complexes

Our EXAFS data suggest that the Se–Fe interatomic distance is 3.33 Å for Se(IV)-adsorbed ferrihydrite, which is similar to previous studies (e.g., Kikuchi et al., 2019). It is noteworthy that spectroscopic measurements are performed on the entire solid, which means that the information obtained from EXAFS analysis could be the mixture of each complexes formed at single surface of minerals. Considering that Se(IV) can be adsorbed at the (1 0 0) and (1 –1 0) faces (~64% and ~36%), we can calculate the average length of the Se–Fe bond for Se(IV) adsorption on ferrihydrite was 3.32 Å, based on the Se–Fe interatomic distances in the bidentate–binuclear (^2C) complexes at the (1 0 0) and (1 –1 0) faces (3.37 Å and 3.21 Å, respectively, predicted by DFT calculations). This consistence in the Se–Fe interatomic distances obtained from EXAFS analysis (3.33 Å) and DFT calculations (3.32 Å) clearly suggests that Se (IV) adsorption could occur at the (1 0 0) facet in addition to dominant (1 –1 0) facet of ferrihydrite with the formation of bidentate–binuclear inner-sphere complexes.

For Se(VI), the EXAFS results indicate that Se(VI) is mainly adsorbed

Table 1
Chemical and isotopic results of Se(IV) adsorption on ferrihydrite.

Experiments	Time (h)	pH	IS (M)	$[Se]_{initial}$ (μM)	Adsorption (%)	Coverage (μmol/m^2)	$\delta^{82/76}Se_{aqueous}$ ‰	2sd ‰	$\delta^{82/76}Se_{adsorbed}$ ‰	2sd ‰	$\Delta^{82/76}Se_{aqueous-adsorbed}$ ‰	2sd ‰
Adsorption kinetic experiment	0.17	7	0.01	38.8	35.1	0.041	−0.82	0.08	−1.85	0.23	1.03	0.24
Time-series set	0.5	7	0.01	38.8	42.6	0.050	−0.79	0.07	−1.71	0.17	0.92	0.18
	1	7	0.01	38.8	52.5	0.062	−0.53	0.12	−1.74	0.16	1.18	0.20
	3	7	0.01	38.8	56.0	0.066	−0.51	0.07	−1.71	0.12	1.20	0.14
	5	7	0.01	38.8	63.1	0.074	−0.35	0.08	−1.66	0.11	1.31	0.13
	12	7	0.01	38.8	68.3	0.080	−0.40	0.08	−1.54	0.10	1.15	0.12
	24	7	0.01	38.8	76.0	0.091	−0.41	0.09	−1.41	0.08	0.99	0.12
	36	7	0.01	38.8	75.9	0.089	−0.53	0.12	−1.39	0.09	0.86	0.15
	48	7	0.01	38.8	76.4	0.090	−0.47	0.09	−1.40	0.08	0.93	0.12
	60	7	0.01	38.8	75.4	0.089	−0.49	0.08	−1.40	0.08	0.91	0.12
	96	7	0.01	38.8	77.3	0.091	−0.50	0.11	−1.38	0.08	0.88	0.14
Adsorption edge experiment	48	4	0.01	38.8	99.7	0.117	−0.24	0.09	−1.18	0.06	0.94	0.11
pH-dependent set	48	5	0.01	38.8	97.3	0.115	−0.30	0.08	−1.20	0.06	0.90	0.10
	48	6	0.01	38.8	91.2	0.107	−0.41	0.12	−1.26	0.07	0.85	0.14
	48	7	0.01	38.8	77.3	0.091	−0.50	0.08	−1.38	0.08	0.88	0.11
	48	8	0.01	38.8	69.3	0.082	−0.59	0.11	−1.44	0.10	0.86	0.15
	48	4	0.7	38.8	97.1	0.114						
	48	5	0.7	38.8	97.2	0.114						
	48	6	0.7	38.8	89.3	0.105						
	48	7	0.7	38.8	75.4	0.089	−0.49	0.08	−1.40	0.08	0.91	0.12
	48	8	0.7	38.8	71.7	0.084	−0.51	0.12	−1.44	0.10	0.93	0.15
Adsorption isotherm experiment	48	7	0.01	0.7	99.3	0.002						
Concentration-control set	48	7	0.01	2.6	99.7	0.008						
	48	7	0.01	6.6	99.6	0.020						
	48	7	0.01	13.0	98.0	0.039	−0.31	0.09	−1.20	0.06	0.89	0.11
	48	7	0.01	25.2	83.5	0.064	−0.41	0.11	−1.33	0.08	0.92	0.13
	48	7	0.01	38.8	73.7	0.087	−0.55	0.08	−1.41	0.09	0.86	0.12
	48	7	0.01	77.7	60.9	0.143	−0.66	0.12	−1.51	0.13	0.85	0.17
	48	7	0.01	260.2	35.0	0.276	−0.86	0.10	−1.77	0.25	0.91	0.27
	48	7	0.7	2.6	98.2	0.008						
	48	7	0.7	6.6	99.5	0.020						
	48	7	0.7	13.0	99.8	0.039						
	48	7	0.7	38.8	82.8	0.097	−0.41	0.09	−1.34	0.08	0.93	0.12
	48	7	0.7	130.1	44.5	0.175	−0.81	0.08	−1.64	0.17	0.82	0.19
	48	7	0.7	260.2	32.6	0.257	−0.91	0.10	−1.74	0.28	0.83	0.29

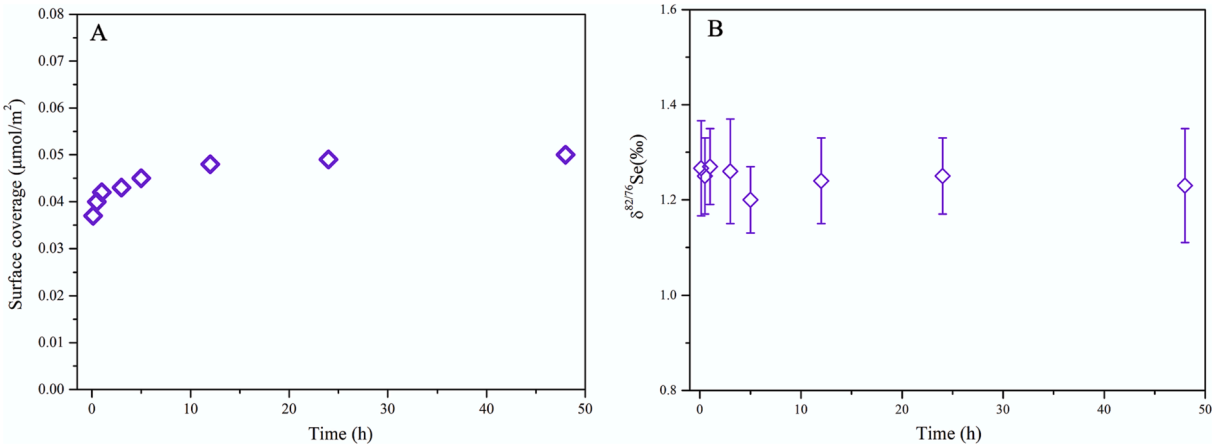

Fig. 3. The surface coverage (A) and aqueous Se isotope composition (B) during Se(VI) adsorption on ferrihydrite.

on 2-line ferrihydrite with the formation of outer-sphere complexes (Fig. 7). Nevertheless, it should be noted that EXAFS is not very sensitive to species comprising roughly 5–10% or less of the total adsorbed species (Foster et al., 2003). That is, if the ratio of inner-sphere complex is very small or negligible compared with predominant outer-sphere complex on ferrihydrite, the contribution of inner-sphere complex may not be reflected by EXAFS analysis. In fact, it remains somewhat debated regarding the adsorption mechanism (inner-sphere or outer-sphere complexation) for Se(VI) on Fe (oxyhydr)oxides (Manceau and Charlet, 1994; Peak and Sparks, 2002; Harada and Takahashi, 2008). The spectroscopic and theoretical studies have given the coherent result that the outer-sphere complexation is the predominant mechanism

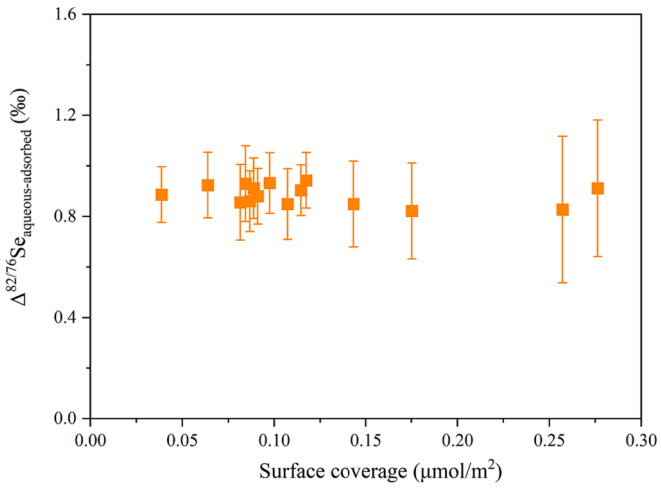

Fig. 4. A plot of Se isotopic fractionations as a function of surface coverages for Se(IV) on ferrihydrite.

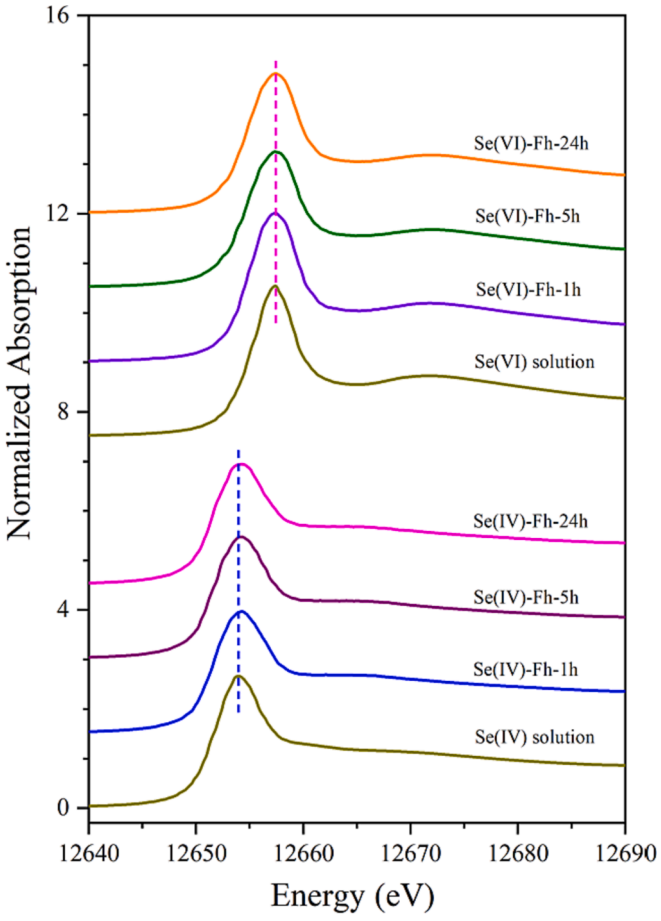

Fig. 5. Se K-edge XANES spectra of adsorbed samples. Blue and red dash lines denote the peak energy of Se(IV) and Se(VI) species, respectively.

except for the systems under acidic and high ionic strength conditions (Wijnja and Schulthess, 2000; Fukushi and Sverjensky, 2007; Harada and Takahashi, 2008; Kikuchi et al., 2019). Our experiments were mainly performed under neutral conditions similar to natural environments, which implies the dominant formation of outer-sphere complexes on the surface of 2-line ferrihydrite, as theoretically predicted by the proton dissociation constants (Qin et al., 2017a). Provided that there is a small amount of Se(VI) inner-sphere complex that cannot be clearly distinguished by EXAFS analysis, but it is not necessary to discuss Se isotope fractionation during Se(VI) adsorption considering its negligible contribution.

4.2.2. *Se isotope fractionation controlled by the structure of surface complexes*

As a classic rule governing stable isotopic fractionation of an element, heavy isotopes are preferentially enriched in the component with stiffer bonding environments (e.g., lower coordination numbers, shorter bond lengths, and highly covalent bonds) when two substances are in equilibrium (Bigeleisen and Mayer, 1947; Schauble, 2004). Our results regarding heavier Se isotopes remaining in the solution during the adsorption on Fe (oxyhydr)oxides likely suggest a stronger and stiffer bonding environment in the aqueous phase compared with the adsorbed Se complexes. This follows the general trend for anionic metal species (e.g., WO_4^{2-} and MoO_4^{2-}) that lighter isotopes are inclined to be distributed to the adsorbed phases on the mineral surfaces (Goldberg et al., 2009; Wasylenki et al., 2011; Kashiwabara et al., 2017).

Given that the oxidation state of Se does not change in our systems, several possible mechanisms are proposed to be responsible for isotope fractionation caused by adsorption. One possible mechanism is the effect of protonation/deprotonation of metal species in solution and on the mineral surface. Nonetheless, this effect appears to be limited, as the dominant dissolved $HSeO_3^-$ and SeO_4^{2-} species can be extensively present at a wide pH range (Fig. S1). Additionally, the first-principles calculations showed that Se isotope fractionation between aqueous SeO_3^{2-} and $HSeO_3^-$ is very small (Li and Liu, 2011), which is not sufficient to explain the larger fractionation during Se(IV) adsorption on Fe (oxyhydr)oxides.

Another possible mechanism is the change of the interatomic distance between the element and its nearest neighbor O atoms, which primarily controls the vibrational frequencies and thus equilibrium isotope fractionation of an element between the aqueous phase and solid phase (Bigeleisen and Mayer, 1947; Schauble, 2004). It has been demonstrated that a larger Zn isotope fractionation for ferrihydrite than goethite is attributed to the degree of change in the Zn–O bond length caused by adsorption (Juillot et al., 2008; Gou et al., 2018). In comparison with aqueous Zn solution (R_{Zn-O} = 2.11 Å), the interatomic distance of the Zn–O bond in Zn-adsorbed ferrihydrite (R_{Zn-O} = 1.96 Å) becomes much shorter than that in Zn-adsorbed goethite (R_{Zn-O} = 2.06 Å). Likewise, Nakada et al. (2013) reported that the isotope fractionations of Nd and Sm are also governed by the shorter REE-O distances in the adsorbed species on δ-MnO_2 relative to their aqua ions. However, in the case of Se, the Se–O bond length is indistinguishable between the solution and the adsorbed phase (i.e., ferrihydrite) from our EXAFS results (Table 2). Hence, Se isotope fractionation during adsorption on Fe (oxyhydr)oxides is not primarily driven by the change of the Se–O bond length.

A third possible mechanism is that the attachment mode and the structure of surface complexes on the minerals govern the isotopic fractionation of an element. It has been suggested that adsorption reaction with outer-sphere complexation does not induce a large isotopic fractionation, because the local structure of the element does not change by the adsorption reaction (Lemarchand et al., 2007; Kashiwabara et al., 2011; Takahashi et al., 2015). Lemarchand et al. (2007) reported a small boron isotope fractionation due to the formation of outer-sphere complexes on the birnessite surface. Kashiwabara et al. (2011) indicated that Mo isotopes cannot be fractionated largely by the outer-sphere complexation during adsorption on ferrihydrite. For Se(VI), a small or negligible Se isotope fractionation (<0.2‰) can be ascribed by the attachment mode of the outer-sphere complexation during adsorption on ferrihydrite, hematite, and clay minerals, as revealed by this work and our earlier studies (Xu et al., 2020, 2021).

However, the formation of inner-sphere complexes on the mineral surfaces generally leads to a relatively large isotope fractionation, as reported for the adsorption of boron on goethite (Lemarchand et al.,

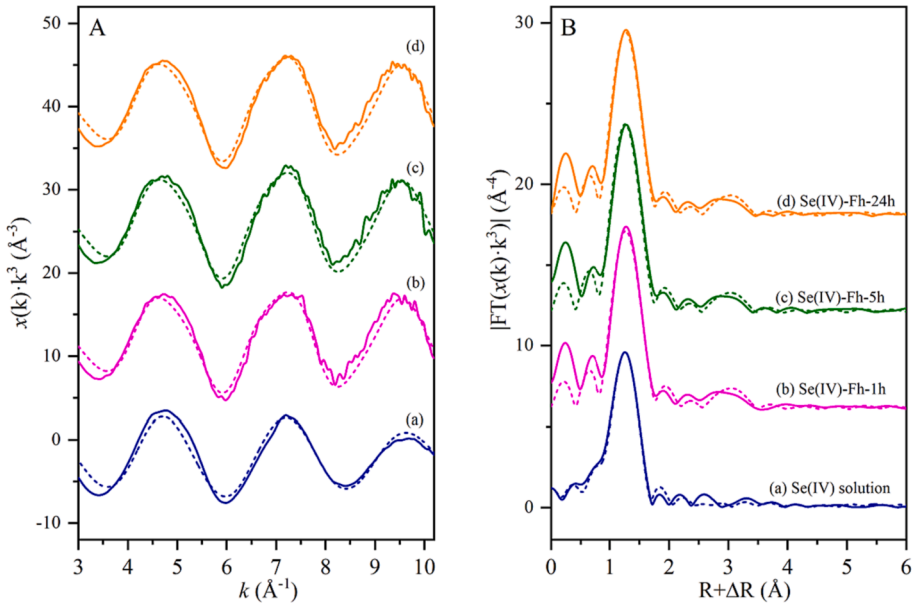

Fig. 6. Se K-edge EXAFS spectra of Se(IV) adsorbed samples (A: k^3-weighted *x(k)* spectra; B: RSFs (phase shift not corrected)). Solid lines are spectra obtained by experiments, and dash lines are calculated spectra by the curve-fitting analysis.

Table 2
Structural parameters of EXAFS spectra for adsorbed samples.

Sample	Shell	CN	R (Å)	ΔE_0(eV)	σ^2 (Å^2)	R factor (%)
Se(IV) solution	Se–O	3.4 (6)	1.69 (1)	8.2 (7)	0.006 (1)	0.88
Se(IV)-Fh-1 h[a]	Se–O	3.2 (6)	1.70 (1)	9.7 (4)	0.003 (1)	0.69
	Se–Fe	1.8 (1)	3.33 (2)		0.012 (3)	
Se(IV)-Fh-5 h	Se–O	3.4 (6)	1.70 (1)	8.9 (5)	0.003 (1)	0.91
	Se–Fe	1.6 (1)	3.33 (2)		0.012 (3)	
Se(IV)-Fh-24 h	Se–O	3.3 (6)	1.70 (1)	9.4 (6)	0.003 (1)	0.70
	Se–Fe	1.8 (1)	3.33 (2)		0.013 (3)	
Se(VI) solution	Se–O	4.1 (7)	1.65 (1)	8.6 (8)	0.001 (1)	0.81
Se(VI)-Fh-1 h	Se–O	3.9 (6)	1.65 (1)	8.7 (9)	0.001 (1)	1.19
Se(VI)-Fh-5 h	Se–O	3.7 (6)	1.65 (1)	8.2 (7)	0.001 (1)	0.90
Se(VI)-Fh-24 h	Se–O	3.8 (6)	1.65 (1)	8.3 (8)	0.001 (1)	0.98

CN, coordination number; R, interatomic distance; ΔE_0, threshold E_0 shift; and σ^2, Debye-Waller factor.
The uncertainties in the last digit for CN, R, ΔE_0, and σ^2 are listed in parentheses.
[a] Se adsorption on ferrihydrite (Fh) at different time.

2007) and Mo on manganese oxides (Kashiwabara et al., 2011). Our results from EXAFS analysis and DFT calculations clearly suggest that Se (IV) predominantly forms bidentate-binuclear corner-sharing (^2C) inner-sphere complexes on the surface of 2-line ferrihydrite, which is expected to induce a substantial Se isotope fractionation. Despite no change in the Se–O bond length as discussed in the foregoing EXAFS results, the formation of the ^2C complexes could lead to symmetry distortion of Se(IV). On the basis of the Se–O bond lengths (1.70 Å) obtained by EXAFS analysis and the distance (R_{O-O} = 2.60 Å) between two O atoms at the Fe (oxyhydr)oxide surface yielded by the formation of the ^2C complex (Manceau, 1995; Pokrovsky et al., 2014), the O–Se–O angle in the adsorbed Se(IV) complex would decrease to 100° relative to that in aqueous Se(IV) species (trigonal pyramidal structure, 107°). This distortion in the O–Se–O angle can decrease the stability of the first coordination sphere (Se–O) in the adsorbed Se, resulting in a substantial enrichment of lighter Se isotopes in the solid phase. This is confirmed by the DFT calculations, showing that theoretical Se(IV) isotope fractionation factor yielded by the formation of the ^2C complex at the (1 0 0) and (1 –1 0) faces of ferrihydrite. This consistency strongly suggests that the small structural distortion caused by the bidentate-binuclear inner-sphere complexation is primarily responsible for equilibrium Se isotope fractionation during Se(IV) adsorption on ferrihydrite (Fig. 11), as demonstrated for Ge isotope fractionation mechanism during the adsorption on goethite (Li and Liu, 2010; Pokrovsky et al., 2014).

4.3. Implication for Se isotope fractionation in natural ferromanganese oxides

Our study demonstrates isotope fractionation behavior and molecular mechanism during Se oxyanions adsorption on 2-line ferrihydrite, which has implications in term of the understanding of Se isotopic composition in marine ferromanganese oxides and reconstructing the global Se cycling in the ocean. Particularly, this study is relevant to hydrogenetic ferromanganese oxides, which can scavenge directly trace elements (including Se) from those dissolved in seawater (Hein and Koschinsky, 2014; Takahashi et al., 2015).

Marine ferromanganese oxide, as an important Se sink, may recover a lot of seawater Se (48%) by the adsorption of Se(IV) (Stüeken, 2017). Koschinsky and Hein, (2003) reported that Se is mainly associated with Fe (oxyhydr)oxide fraction in hydrogenetic samples by a sequential leaching method. Nonetheless, Se speciation and distribution in marine ferromanganese oxides has not been directly determined due to low Se content and strong interference from other elements (particularly Fe and Mn) during measurement by synchrotron-based techniques (e.g., μ-XRF and XAFS). We rationally supposed here that Se in hydrogenetic sample is predominantly present as Se(IV) adsorbed by ferrihydrite with the formation of bidentate-binuclear inner-sphere complexes. This is because (i) hydrogenetic ferromanganese crusts and nodules generally have a higher Fe/Mn ratio, and ferrihydrite is the predominant Fe component (Goldberg et al., 2009; Hein and Koschinsky, 2014; Qin et al., 2019); (ii) Se has a high sorption affinity for ferrihydrite than other constituent minerals such as Mn oxides (Balistrieri and Chao 1990;

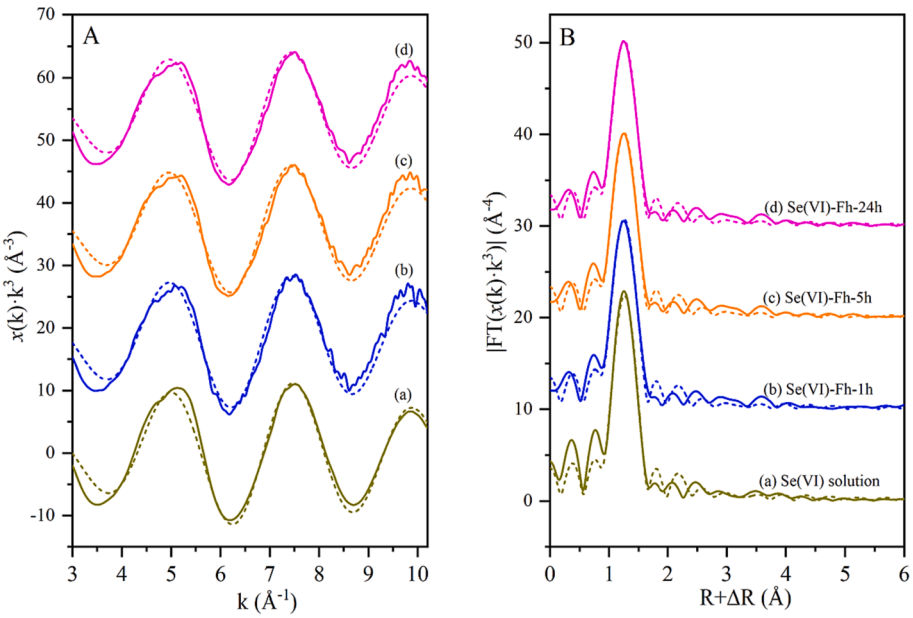

Fig. 7. Se K-edge EXAFS spectra of Se(VI) adsorbed samples (A: k^3-weighted *x(k)* spectra; B: RSFs (phase shift not corrected)). Solid lines are spectra obtained by experiments, and dash lines are calculated spectra by the curve-fitting analysis.

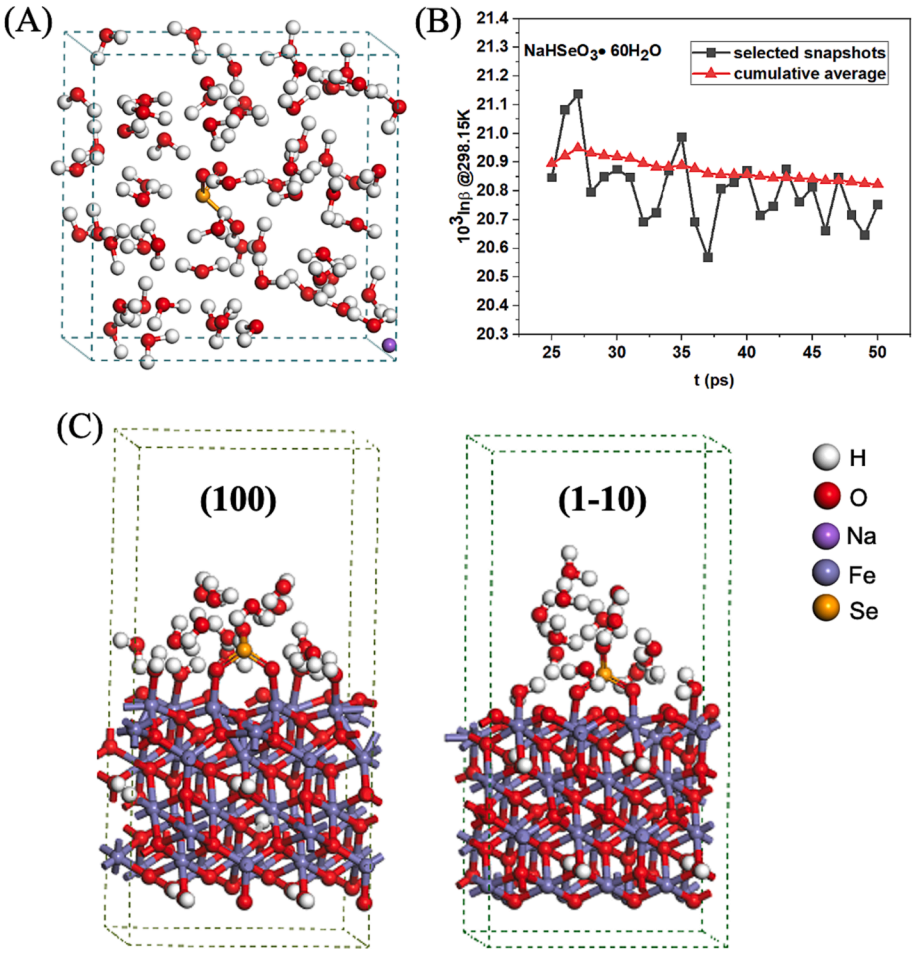

Fig. 8. (A) The first-principles molecular dynamics (FPMD) simulations for Se(IV) aqueous solutions. (B) The calculated reduced partition function ratios (10^3 lnβ) of the selected snapshots and their cumulative average values for each solution at 298.15 K. (C) Optimized structures of bidentate binuclear complexes of Se(IV) on the Fh(100) and (1-10) surfaces.

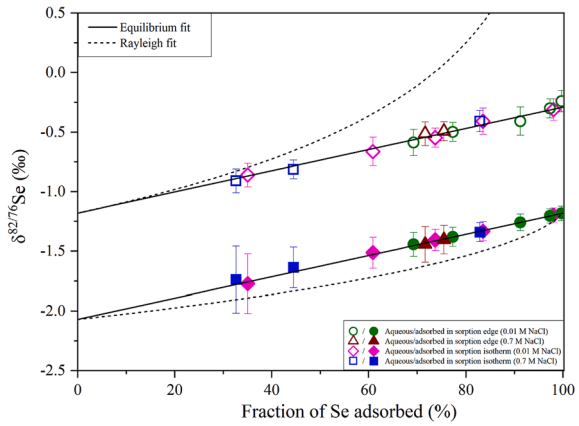

Fig. 9. A plot of $\delta^{82/76}$Se value of aqueous and adsorbed species as a function of the fraction of Se(IV) adsorbed on ferrihydrite.

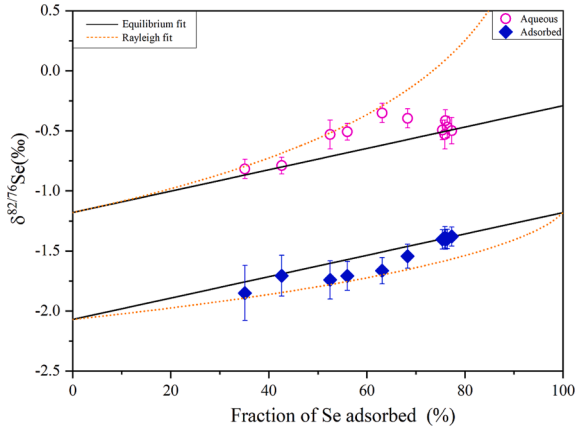

Fig. 10. A plot of $\delta^{82/76}$Se value of aqueous and adsorbed species as a function of the fraction of adsorbed Se(IV) in the kinetic adsorption experiment.

Harada and Takahashi, 2008); and (iii) despite the presence of both Se (VI) and Se(IV) species in the ocean, the affinity of Se(IV) for Fe oxides is much higher in comparison with Se(VI), which is ascribed by the fact Se (IV) can be strongly adsorbed on minerals via the inner-sphere complexation, but Se(VI) forms weak outer-sphere complexes. Although the oxidation of Se(IV) by synthetic Mn oxides has been observed at low pH (Scott and Morgan, 1996; Dwivedi et al., 2022), similar studies also reported incomplete (Banerjee and Nesbitt, 2000) or no Se(IV) oxidation (Balistrieri and Chao, 1990, Foster et al., 2003; Pettine et al., 2013; Xu et al., 2020). XPS and EXAFS results indicated that the formation of Mn(III) can inhibit or slow Se(IV) oxidation (Banerjee and Nesbitt, 2000; Foster et al., 2003), and the continued reaction may passivate the Mn oxide surface (Frierdich and Catalano, 2012). These results indicate that this oxidation of Se(IV) by Mn oxides should be very slow and limited in particular at higher pHs. Furthermore, natural minerals may not be as oxidizing as synthetic phases, which may increase the retention of Se(IV) species due to greater adsorption to Fe and Mn oxides for Se(IV) than Se(VI) (Frierdich and Catalano, 2012). Indeed, Se(IV) has been found to be the predominant Se species in natural cave ferromanganese oxides (Frierdich and Catalano, 2012). Similarly, in the marine environment at the relatively high pH, Se(VI) oxidized from Se(IV) by Mn oxides can be very small. Thus, Se is expected to be predominantly associated with ferrihydrite in the form of Se(IV) in hydrogenetic ferromanganese oxides, while Se(VI) or other Se species could be much smaller. In view of this, we hypothesize here that Se isotope fractionations in hydrogenetic ferromanganese oxides and seawater are primarily controlled by Se(IV) adsorption on ferrihydrite.

Rouxel et al. (2002) firstly reported Se isotopic composition in one Mn nodule (NOD-P-1, USGS standard) from the Pacific Ocean, with the $\delta^{82/76}$Se value of 0.36 ± 0.20‰. They suggested that Se isotopic composition of ferromanganese nodules may approximate that of seawater. Recently, Chang et al. (2017) developed a method for the determination of Se isotopes in seawater and directly determined Se isotopic composition of inorganic Se in seawater from Northwestern Pacific Ocean (with the $\delta^{82/76}$Se ranging from 0.41‰ to 1.59‰), indicating that Se isotopic composition of Mn nodules cannot approximate the overall Se isotopic composition of seawater but only near the ocean

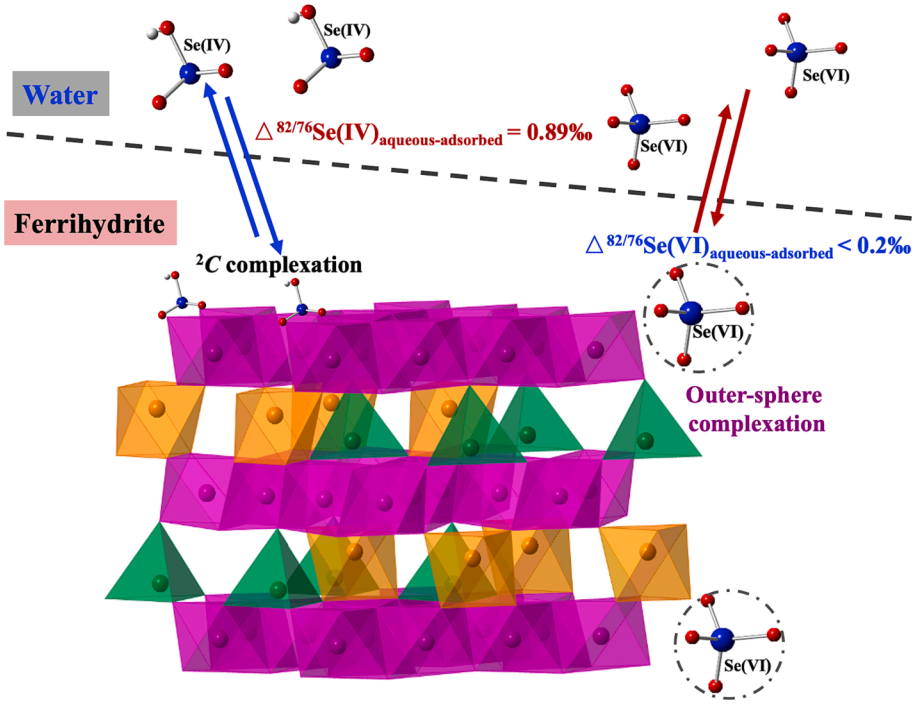

Fig. 11. A schematic diagram showing the molecular-scale mechanism for Se isotope fractionation caused by Se(IV) and Se(VI) adsorption on ferrihydrite.

floor. Assuming dissolved Se isotope composition of seawater in the location of NOD-P-1 is close to those in the ocean floor in Northwestern Pacific Ocean (~0.41‰) reported by Chang et al. (2017), it likely that lighter Se isotopes are slightly enriched in ferromanganese nodules relative to seawater. This could be supported by our experimental results that lighter Se isotopes are preferentially distributed to the solid phase (ferrihydrite) during adsorption. Nevertheless, the magnitude of fractionation (~0.05‰) between seawater and the ferromanganese sample (Rouxel et al., 2002) appears to be smaller than those obtained from Se (IV) adsorption experiment (~0.89‰). One possibility is that the experiment conditions may be different from complex marine environment. Some environmental factor (e.g., co-existing ions) that may result in a change in Se isotope fractionation should be also considered and checked in future. Another possible explanation is that the *syn*-depositional and post-depositional alterations may have an effect on Se isotope composition in ferromanganese oxides. Gueguen et al. (2016) have proposed that Ni isotope variations in different ferromanganese crusts may be influenced by post-depositional processes depending on the growth history and geological settings. The third explanation is that Se isotope fractionation in ferromanganese oxides may be also affected by the adsorption and oxidation of Mn oxides apart from ferrihydrite. It has been indicated that Se could be also immobilized by Mn oxides especially when minor Fe (oxyhydr)oxide is available in ferromanganese sediments (Koschinsky and Hein, 2003). This means that some of Se may be also entrapped by Mn oxides in the NOD-P-1, since this sample is the mixed type of hydrogenetic and diagenetic, with a relatively lower Fe content (Fe/Mn = 0.20) (Flanagan and Gottfried, 1980; Hein and Koschinsky, 2014). Although Se isotope fractionations have been observed for Se(IV) adsorption and oxidation by Mn oxides at low pHs (pH < 5.5; Xu et al., 2020; Dwivedi et al., 2022), Mn oxide adsorption could not cause a strong Se isotope fractionation in the pH range of the ocean (i.e., no Se fractionation at pH 8; Xu et al., 2020), which is significantly disparate from Mo isotope that is very sensitive to Mn oxides (Kashiwabara et al., 2011; Wasylenki et al., 2011). This probably suggests that Se isotope fractionation is relatively small to seawater for the ferromanganese oxides containing more Mn minerals. Further detailed studies of Se isotope compositions in different type of ferromanganese oxides (i.e., hydrogenetic, diagenetic, and hydrothermal type) and deep seawater are required to clarify the relationship between the $\delta^{82/76}$Se in ferromanganese oxides and seawater.

Taking into account a substantial fractionation during Se(IV) adsorption observed in this study, Se isotope fractionation caused by various biogeochemical processes like adsorption should be considered to deduce the Se isotope information in ancient seawater from ferromanganese oxides. In combination with mineralogy and molecular speciation information of Se in ferromanganese oxides, Se isotope fractionation behavior during adsorption revealed here would lead to the potential application of Se isotope systematics as a proxy of the evolution of Se in the ocean. However, this proxy should be cautiously applied in the Precambrian when the ocean was strongly stratified and some Se may have been produced by reduction in the water column (Stüeken et al., 2015; Stüeken, 2017). Because the reduction of Se can cause much larger fractionation by either abiotic or biotic processes (Herbel et al., 2000; Stüeken, 2017; Schilling et al., 2020), probably superimposing the Se isotope signal caused by adsorption.

4.4. Implication for isotope fractionations of metal oxyanions caused by adsorption

This study elucidates the molecular mechanism driving Se isotope fractionation during Se(IV) and Se(VI) oxyanions adsorption on Fe (oxyhydr)oxides, which also has a significant implication for the understanding of isotope fractionation mechanism for other metal oxyanions during adsorption. That is, different magnitude of isotope fractionations for metal oxyanions can be systematically understood by their local structure of the surface complex formed on the solid phase. As shown in Fig. 12, the extent of equilibrium isotope fractionation of metal oxyanions could be preliminarily assessed by the identification of attachment modes (i.e., inner-sphere or outer-sphere complexation) on the mineral surfaces. Specifically, metal oxyanions (e.g., S(VI), Se(VI), and Cr(VI)) that are adsorbed on the mineral surfaces with the formation of outer-sphere complexes induce a small or negligible isotope fractionation, which can be attributed to no change in their coordination environments by the adsorption reaction. By contrast, a larger fractionation is observed for metal oxyanions (e.g., Ge(IV), Si(IV), and Mo (IV)) forming inner-sphere complexes, in which their local structures have changed compared with dissolved oxyanions. The attachment mode for metal oxyanions by minerals can be identified by EXAFS analysis (Kashiwabara et al., 2011, 2017; Takahashi et al., 2015; Qin et al., 2017a) and/or predicted by the proton dissociation constants (pK_a) of their conjugate acid (Qin et al., 2017a). Generally, the oxyanions with the average pK_a values larger than that of H_2WO_4 are inclined to be adsorbed on the mineral surface via the inner-sphere complexation, whereas those having lower average pK_a values tend to form outer-sphere complexes.

It has been indicated recently that the occurrence of geometrical change from tetrahedral (*Td*) to octahedral (*Oh*) during adsorption is correlated to the radius ratio ($\rho = r_{cation}/r_{anion}$, where r_{cation} and r_{anion} are the ionic radius of the cation and O^{2-}, respectively) of the metal oxyanion, as the maximum coordination number of an ion generally increases with increasing ionic radius (Tanaka et al., 2018). In general, the d^0 and d^{10} ions with large ligands tend to exhibit *Td* geometry (Huheey, 1983; Tanaka et al., 2018). For example, dissolved Cr(VI), Mo (VI), and W(VI) species show the *Td* coordination structures because of their d^0 electron configuration, and the d^{10} metal oxyanions such as Ge (IV), Se(VI), and Se(IV) also exhibit the *Td* or trigonal pyramidal (*Tp*) geometry. The threshold value of the radius ratio (ρ) for the formation of the *Oh* geometry from the *Td* geometry is 0.414, which is derived from the close-packed crystal structure of binary compounds (Rohrer, 2001, Tanaka et al., 2018).

Fig. 12 summarizes the correlation between the radius ratio (ρ) and isotope fractionation factor for some metal oxyanions. The radius ratios of S(VI) (0.230), Se(VI) (0.333), and Cr(VI) (0.349) are significantly lower than the threshold ρ value (0.414), implying that it is unlikely to adopt the *Oh* geometry for these *Td* oxyanions during adsorption. Accordingly, a small or negligible isotope fractionations are observed for these metal oxyanions, which is also consistent with the foregoing prediction from their binding mode of outer-sphere complexation.

By contrast, the Mo(VI) oxyanion that has a greater radius ratio (0.468) than the boundary (0.414) shows a substantial Mo isotope fractionation during adsorption on Fe and Mn (oxyhydr)oxides. It has been suggested recently that the *Td* MoO_4^{2-} species with vacant Mo $4d^0$ orbital can accept electron donations from the $-O^-$/–OH groups on the surface of Mn oxide to form the surface complex with highly distorted *Oh* geometry, causing a larger Mo isotope fractionation (Tanaka et al., 2018). Kashiwabara et al. (2011) demonstrated the magnitude of Mo fractionation ($^{98/95}$Mo) is closely linked to the proportion of the *Oh* species in the surface complexes on different minerals, with the systematic tendency of ferrihydrite (0.37‰ amu^{-1}, 0% *Oh*) < goethite (0.47‰ amu^{-1}, 54% *Oh*) < hematite (0.73‰ amu^{-1}, 86% *Oh*) < δ-MnO_2 (0.97‰ amu^{-1}, 100% *Oh*). Surprisingly, W isotope fractionation is not so large as those for Mo and V, although the greater radius ratio of WO_4^{2-} (0.476) allows the formation of the *Oh* surface complexes. This discrepancy can be explained by different distortion extent of *Oh* complexes at the mineral surface. Indeed, previous EXAFS results suggested a highly distorted *Oh* symmetry for adsorbed Mo complexes relative to W, with a clear split in the Mo-O shell for Mo-adsorbed materials but only a single broad W-O shell for W-adsorbed samples (Kashiwabara et al., 2011, 2013).

For Se(IV) and Ge(IV) oxyanions with the ρ values close to the threshold (Se(IV): 0.397; Ge(IV): 0.421), the two anionic species with fully occupied d^{10} orbits prefer to maintain the trigonal or *Td* geometry

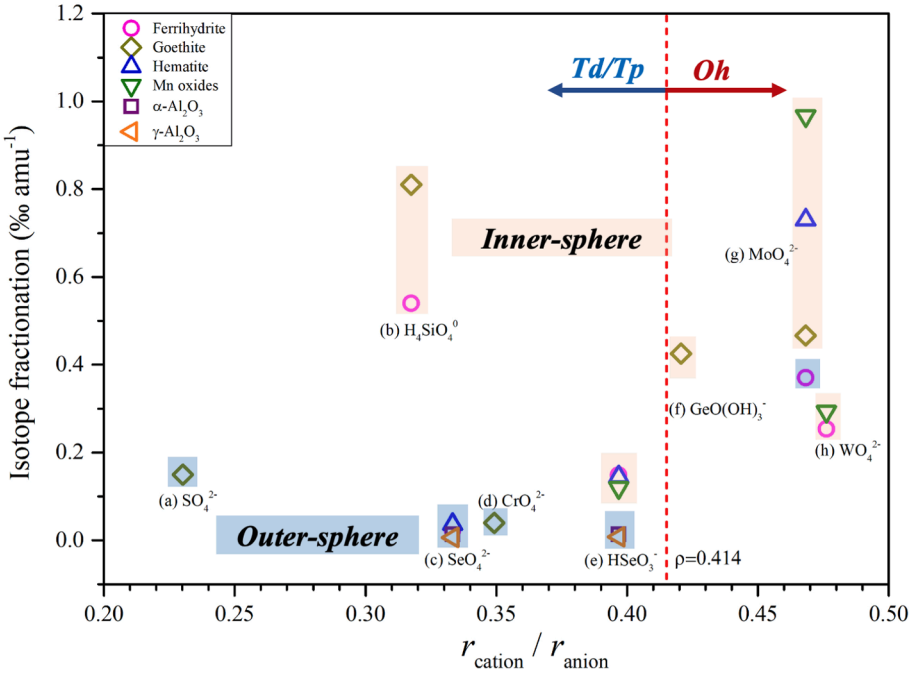

Fig. 12. A summary plot of the correlation between the radius ratio (ρ) and isotope fractionation of metal oxyanions during adsorption on different minerals (Blue and orange shadows represent outer-sphere and inner-sphere complexation, respectively). a: S(VI) adsorption on goethite ($^{34/32}$S; Van Stempvoort et al., 1990). b: Aqueous monosilicic acid ($H_4SiO_4^0$) adsorption on ferrihydrite and goethite ($^{29/28}$Si; Delstanche et al., 2009). c: Se(VI) adsorption on ferrihydrite from this study ($^{82/76}$Se), while Se(VI) adsorption on hematite and Al oxides is cited from Xu et al. (2020). d: Cr(VI) adsorption on goethite ($^{53/52}$Cr; Ellis et al., 2004) e: Se(IV) adsorption on ferrihydrite from this study ($^{82/76}$Se), while Se(IV) adsorption on hematite, Mn and Al oxides is cited from Xu et al. (2020). f: Ge(IV) adsorption on goethite ($^{74/70}$Ge; Pokrovsky et al., 2014). g: Mo(VI) adsorption on Fe (oxyhydr)oxides ($^{98/95}$Mo; Goldberg et al., 2009) and Mn oxides ($^{98/95}$Mo; Barling and Anbar, 2004). h: W (VI) adsorption on ferrihydrite and Mn oxide ($^{186/183}$Mo; Kashiwabara et al., 2017).

at the mineral surfaces during adsorption. However, the formation of the ^2C complexes can lead to the change in the O-Se/Ge-O angle and thus the distortion of the *Td/Tp* geometry. This distortion can induce a substantial isotope fractionation during adsorption on Fe (oxyhydr)oxides, as discussed in detail in the foregoing Section 4.2 and a previous study (Pokrovsky et al., 2014). The larger isotope fractionation for Ge(IV) (0.42‰ amu^{-1}, $^{74/70}$Ge) than Se(IV) (0.15‰ amu^{-1}, $^{82/76}$Se) is likely due to the higher distortion for Ge(IV) bidentate-binuclear complex, with a greater change in the O–Ge–O angle (14.5°, Pokrovsky et al., 2014) than the O–Se–O angle (7°, this study) after adsorption reaction.

Herein, we propose a new insight into the systematical understanding of mechanisms governing equilibrium isotope fractionations of metal oxyanions caused by adsorption, on the basis of their proton dissociation constant, electronic configuration, and radius ratio. The systematical tendency for the isotope fractionation of metal oxyanions during adsorption can be summarized as follows: (i) formation of outer-sphere complexes causes a small or insignificant isotope fractionation; (ii) the magnitude of isotope fractionations for the oxyanions forming inner-sphere complexes is primarily controlled by the distortion degree in the *Td/Tp* structure of the surface complexes relative to aqueous species; and (iii) much larger isotope fractionations can be observed for the oxyanions whose structure can change from *Td* to *Oh* geometry. Considering the mixture of specific phases in natural samples, this molecular-scale knowledge regarding isotopic fractionation between dissolved oxyanions and the adsorbed sinks has important implications with regard to the interpretation of natural isotope signatures of metal oxyanions in modern and ancient environments.

5. Conclusions

This study clarifies the molecular mechanism responsible for equilibrium Se isotope fractionation during adsorption on 2-line ferrihydrite by combining experimental measurements, DFT calculations, and EXAFS analyses. Se isotopes can be substantially fractionated during Se (IV) adsorption on Fe (oxyhydr)oxides with lighter Se isotopes being preferentially distributed to the solid phase, which is driven by the formation of distorted bidentate-binuclear inner-sphere complexes. By contrast, adsorption of Se(VI) causes a small or negligible Se isotope fractionation due to the outer-sphere complexation. Our results would provide molecular-scale insights into the application of Se isotope as a potential paleo-oceanographic proxy. Furthermore, the findings presented here have significant implications for the systematical understanding of mechanisms controlling equilibrium isotopic fractionations of other metal oxyanions during adsorption, which may help interpret isotope signatures of metal oxyanions in the dissolved species and the adsorbed sinks in natural environments.

Declaration of Competing Interest

The authors declare that they have no known competing financial interests or personal relationships that could have appeared to influence the work reported in this paper.

Acknowledgments

This work was supported by the National Natural Science Foundation of China (Nos. 42373025 and U1732132), the Pioneer Hundred Talents Program of Chinese Academy of Sciences, Guizhou Provincial Science and Technology Projects (No. ZK[2023]051), and JSPS KAKENHI (Nos. 20K15204 and 17F17332). We thank Prof. Thomas M. Johnson at the University of Illinois Urbana-Champaign, Dr. Qi Liu, Caihong Gao, and Feixiang Liu at Institute of Geochemistry, Chinese Academy of Sciences for valuable discussion. The XAFS spectra were collected at the BL14W1 beamline of the Shanghai Synchrotron Radiation Facility and the 1W1B beamline of Beijing Synchrotron Radiation Facility.

Appendix A. Supplementary material

Supplemental figures showing Se species in solution as a function of pH, the radial distribution functions g(r) for Se–O pair in HSeO3 the effect of the calculated region of surface models on vibration frequencies, and Eh-pH diagram of Se and Fe. Supplemental table showing the results of Se(VI) adsorption on ferrihydrite. Supplementary material to this article can be found online at https://doi.org/10.1016/j.gca.2023.09.009.

References

Balistrieri, L.S., Chao, T.T., 1990. Adsorption of selenium by amorphous iron oxyhydroxide and manganese dioxide. Geochim. Cosmochim. Acta 54, 739–751.

Balistrieri, L.S., Borrok, D.M., Wanty, R.B., Ridley, W.I., 2008. Fractionation of Cu and Zn isotopes during adsorption onto amorphous Fe(III) oxyhydroxide: Experimental mixing of acid rock drainage and ambient river water. Geochim. Cosmochim. Acta 72, 311–328.

Banerjee, D., Nesbitt, H.W., 2000. XPS study of reductive dissolution of birnessite by H_2SeO_3 with constraints on reaction mechanism. Am. Mineral. 85, 817–825.

Barling, J., Anbar, A.D., 2004. Molybdenum isotope fractionation during adsorption by manganese oxides. Earth Planet. Sci. Lett. 217, 315–329.

Bigeleisen, J., Mayer, M.G., 1947. (1947) Calculation of equilibrium constants for isotopic exchange reactions. J. Chem. Phys. 15, 261–267.

Brazier, J.M., Schmitt, A.D., Gangloff, S., Pelt, E., Chabaux, F., Tertre, E., 2019. Calcium isotopic fractionation during adsorption onto and desorption from soil phyllosilicates (kaolinite, montmorillonite and muscovite). Geochim. Cosmochim. Acta 250, 324–347.

Brookins, D.G., 1988. Eh-pH Diagrams for Geochemistry. Springer-Verlag, Berlin, p. 176.

Catalano, J.G., Zhang, Z., Fenter, P., Bedzyk, M.J., 2006. Inner-sphere adsorption geometry of Se(IV) at the hematite (100)-water interface. J. Colloid Interface Sci. 297, 665–671.

Chang, Y., Zhang, J., Qu, J.Q., Xue, Y., 2017. Precise selenium isotope measurement in seawater by carbon-containing hydride generation-Desolvation-MC-ICP-MS after thiol resin preconcentration. Chem. Geol. 471, 65–73.

Chappell, H.F., Thom, W., Bowron, D.T., Faria, N., Hasnip, P.J., Powell, J.J., 2017. Structure of naturally hydrated ferrihydrite revealed through neutron diffraction and first-principles modeling. Phys. Rev. Mater. 1, 036002.

Cutter, G.A., Bruland, K.W., 1984. The marine biogeochemistry of selenium: A re-evaluation1. Limnol. Oceanogr. 29, 1179–1192.

Cutter, G.A., Cutter, L.S., 2001. Sources and cycling of selenium in the western and equatorial Atlantic Ocean. Deep-Sea Res. II 48, 2917–2931.

Delstanche, S., Opfergelt, S., Cardinal, D., Elsass, F., Andre, L., Delvaux, B., 2009. Silicon isotopic fractionation during adsorption of aqueous monosilicic acid onto iron oxide. Geochim. Cosmochim. Acta 73, 923–934.

Dong, S., Wasylenki, L.E., 2016. Zinc isotope fractionation during adsorption to calcite at high and low ionic strength. Chem. Geol. 447, 70–78.

Dwivedi, P., Schilling, K., Wasserman, N., Johnson, T.M., Pallud, C., 2022. Oxidation of dissolved tetravalent selenium by birnessite: Se isotope fractionation and the effects of pH and birnessite structure. Front. Earth Sci. 10, 909900.

Ellis, A.S., Johnson, T.M., Bullen, T.D., 2004. Using chromium stable isotope ratios to quantify Cr(VI) reduction: Lack of sorption effects. Environ. Sci. Technol. 38, 3604–3607.

Flanagan, F.J., Gottfried, D., 1980. US Geol. Surv. Rock Standards: III. Manganese nodule reference samples USGS-NOD-A-1 and USGS-NOD-P-1. USGS Prof. Pap. 1155.

Foster, A.L., Brown, G.E., Parks, G.A., 2003. X-ray absorption fine structure study of As (V) and Se(IV) sorption complexes on hydrous Mn oxides. Geochim. Cosmochim. Acta 67, 1937–1953.

Frierdich, A.J., Catalano, J.G., 2012. Distribution and speciation of trace elements in iron and manganese oxide cave deposits. Geochim. Cosmochim. Acta 91, 240–253.

Fukushi, K., Sverjensky, D.A., 2007. A surface complexation model for sulfate and selenate on iron oxides consistent with spectroscopic and theoretical molecular evidence. Geochim. Cosmochim. Acta 71, 1–24.

Gao, C., Liu, Y., 2021. First-principles calculations of equilibrium bromine isotope fractionations. Geochim. Cosmochim. Acta 297, 65–81.

Giester, G., 1996. Crystal structure of $Fe_2O(SeO_3)_2$, a new oxoselenite compound with ferric iron in distorted tetrahedral coordination. Z. Kristallogr. 211, 603–606.

Giester, G., Wildner, M., 1991. Synthesis and crystal structure of monoclinic $Fe_2(SeO_4)_3$. Monatsh. Chem. 122, 617–623.

Goldberg, T., Archer, C., Vance, D., Poulton, S.W., 2009. Mo isotope fractionation during adsorption to Fe (oxyhydr)oxides. Geochim. Cosmochim. Acta 73, 6502–6516.

Gou, W., Li, W., Ji, J., Li, W., 2018. Zinc isotope fractionation during sorption onto al oxides: Atomic level understanding from EXAFS. Environ. Sci. Technol. 52, 9087–9096.

Grimme, S., Antony, J., Ehrlich, S., Krieg, H., 2010. A consistent and accurate ab initio parametrization of density functional dispersion correction (DFT-D) for the 94 elements H-Pu. J. Chem. Phys. 132, 154104.

Gueguen, B., Rouxel, O., Rouget, M.-L., Bollinger, C., Ponzevera, E., Germain, Y., Fouquet, Y., 2016. Comparative geochemistry of four ferromanganese crusts from the Pacific Ocean and significance for the use of Ni isotopes as paleoceanographic tracers. Geochim. Cosmochim. Acta 189, 214–235.

Gueguen, B., Sorensen, J.V., Lalonde, S.V., Peña, J.T., Brandy, M., Rouxel, O., 2018. Variable Ni isotope fractionation between Fe-oxyhydroxides and implications for the use of Ni isotopes as geochemical tracers. Chem. Geol. 481, 38–52.

Gustafsson, J.P., 2018. Visual MINTEQ, version 3.1; Department of Land and Water Resources Engineering, KTH (Royal Institute of Technology): Stockholm. Available for free download at the website of http://vminteq.lwr.kth.se/download/.

Halevy, I., Bachan, A., 2017. The geologic history of seawater pH. Science 355, 1069–1071.

Harada, T., Takahashi, Y., 2008. Origin of the difference in the distribution behavior of tellurium and selenium in a soil-water system. Geochim. Cosmochim. Acta 72, 1281–1294.

Hayes, K.F., Roe, A.L., Brown, G.E., Hodgson, K.O., Leckie, J.O., Parks, G.A., 1987. In situ x-ray absorption study of surface complexes selenium oxyanions on α-FeOOH. Science 238, 783–786.

Hein, J.R., Koschinsky, A., 2014. Deep-ocean ferromanganese crusts and nodules. In: Holland, H.D., Turekian, K.K. (Eds.), Treatise on Geochemistry, second ed. Elsevier, Oxford, pp. 273–291.

Herbel, M.J., Johnson, T.M., Oremland, R.S., Bullen, T.D., 2000. Fractionation of selenium isotopes during bacterial respiratory reduction of selenium oxyanions. Geochim. Cosmochim. Acta 64, 3701–3709.

Hiemstra, T., 2013. Surface and mineral structure of ferrihydrite. Geochim. Cosmochim. Acta 105, 316–325.

Huheey, J.E., 1983. Inorganic Chemistry: Principles of Structure and Reactivity, third ed. Harper & Row, New York.

Johnson, T.M., Bullen, T.D., 2003. Selenium isotope fractionation during reduction by Fe (II)-Fe(III) hydroxide-sulfate (green rust). Geochim. Cosmochim. Acta 67, 413–419.

Johnson, T.M., Bullen, T.D., 2004. Mass-dependent fractionation of selenium and chromium isotopes in low-temperature environments. Rev. Mineral. Geochem. 55, 289–317.

Johnson, T.M., Herbel, M.J., Bullen, T.D., 1999. Selenium isotope ratios as indicators of selenium sources and oxyanion reduction. Geochim. Cosmochim. Acta 63, 2775–2783.

Johnson, T.M., Bullen, T.D., Zawislanski, P.T., 2000. Selenium stable isotope ratios as indicators of sources and cycling of selenium results from the northern reach of San Francisco bay. Environ. Sci. Technol. 34, 2075–2079.

Juillot, F.C., Marechal, C., Ponthieu, M., Cacaly, S., Morin, G., Benedetti, M., Hazemann, J.L., Proux, O., Guyot, F., 2008. Zn isotopic fractionation caused by sorption on goethite and 2-lines ferrihydrite. Geochim. Cosmochim. Acta 72, 4886–4900.

Kashiwabara, T., Takahashi, Y., Tanimizu, M., Usui, A., 2011. Molecular-scale mechanisms of distribution and isotopic fractionation of molybdenum between seawater and ferromanganese oxides. Geochim. Cosmochim. Acta 75, 5762–5784.

Kashiwabara, T., Takahashi, Y., Marcus, M.A., Uruga, T., Tanida, H., Terada, Y., Usui, A., 2013. Tungsten species in natural ferromanganese oxides related to its different behavior from molybdenum in oxic ocean. Geochim. Cosmochim. Acta 106, 364–378.

Kashiwabara, T., Oishi, Y., Sakaguchi, A., Sugiyama, T., Usui, A., Takahashi, Y., 2014. Chemical processes for the extreme enrichment of tellurium into marine ferromanganese oxides. Geochim. Cosmochim. Acta 131, 150–163.

Kashiwabara, T., Kubo, S., Tanaka, M., Senda, R., Iizuka, T., Tanimizu, M., Takahashi, Y., 2017. Stable isotope fractionation of tungsten during adsorption on Fe and Mn (oxyhydr)oxides. Geochim. Cosmochim. Acta 204, 52–67.

Kikuchi, S., Kashiwabara, T., Shibuya, T., Takahashi, Y., 2019. Molecular-scale insights into differences in the adsorption of cesium and selenium on biogenic and abiogenic ferrihydrite. Geochim. Cosmochim. Acta 251, 1–14.

Kipp, M.A., Stueken, E.E., Bekker, A., Buick, R., 2017. Selenium isotopes record extensive marine suboxia during the Great Oxidation Event. PNAS 114, 875–880.

König, S., Eickmann, B., Zack, T., Yierpan, A., Wille, M., Taubald, H., Schoenberg, R., 2019. Redox induced sulfur-selenium isotope decoupling recorded in pyrite. Geochim. Cosmochim. Acta 244, 24–39.

Koschinsky, A., Hein, J.R., 2003. Uptake of elements from seawater by ferromanganese crusts: solid-phase associations and seawater speciation. Mar. Geol. 198, 331–351.

Kubicki, J.D., Paul, K.W., Kabalan, L., Zhu, Q., Mrozik, M.K., Aryanpour, M., Pierre-Louis, A.M., Strongin, D.R., 2012. ATR-FTIR and density functional theory study of the structures, energetics, and vibrational spectra of phosphate adsorbed onto goethite. Langmuir 28, 14573–14587.

Kubicki, J.D., Kabengi, N., Chrysochoou, M., Bompoti, N., 2018. Density functional theory modeling of chromate adsorption onto ferrihydrite nanoparticles. Geochem. Trans. 19, 8.

Labidi, J., König, S., Kurzawa, T., Yierpan, A., Schoenberg, R., 2018. The selenium isotopic variations in chondrites are mass-dependent; implications for sulfide formation in the early solar system. Earth Planet. Sci. Lett. 481, 212–222.

Large, R.R., Halpin, J.A., Lounejeva, E., Danyushevsky, L.V., Maslennikov, V.V., Gregory, D., Sack, P.J., Haines, P.W., Long, J.A., Makoundi, C., Stepanov, A.S., 2015. Cyclesofnutrient trace elements in the Phanerozoic Ocean. Gondwana Res. 28, 1282–1293.

Lemarchand, E., Schott, J., Gaillardet, J., 2007. How surface complexes impact boron isotope fractionation: Evidence from Fe and Mn oxides sorption experiments. Earth Planet. Sci. Lett. 260, 277–296.

Lenz, M., Lens, P.N.L., 2009. The essential toxin: The changing perception of selenium in environmental sciences. Sci. Total Environ. 407, 3620–3633.

Li, X.F., Liu, Y., 2010. First-principles study of Ge isotope fractionation during adsorption on Fe(III)-oxyhydroxide surfaces. Chem. Geol. 278, 15–22.

Li, X.F., Liu, Y., 2011. Equilibrium Se isotope fractionation parameters: A first-principles study. Earth Planet. Sci. Lett. 304, 113–120.

Li, W., Liu, X.M., Hu, Y., Teng, F.-Z., Hu, Y.-F., 2021. Potassium isotopic fractionation during clay adsorption. Geochim. Cosmochim. Acta 304, 160–177.
Little, S.H., Sherman, D.M., Vance, D., Hein, J.R., 2014. Molecular controls on Cu and Zn isotopic fractionation in Fe–Mn crusts. Earth Planet. Sci. Lett. 396, 213–222.
Manceau, A., 1995. The mechanism of anion adsorption on iron oxides: Evidence for the bonding of arsenate tetrahedra on free $Fe(O, OH)_6$ edges. Geochim. Cosmochim. Acta 59, 3647–3653.
Manceau, A., Charlet, L., 1994. The mechanism of selenate adsorption on goethite and hydrous ferric oxide. J. Colloid Interface Sci. 168, 87–93.
Mathew, K., Sundararaman, R., Letchworth-Weaver, K., Arias, T.A., Hennig, R.G., 2014. Implicit solvation model for density-functional study of nanocrystal surfaces and reaction pathways. J. Chem. Phys. 140, 084106.
Mitchell, K., Mason, P.R.D., Cappellen, P.V., Johnson, T.M., Twill, B.C., Owens, J.D., Diaz, J., Ingall, E.D., Reichart, G.J., Lyons, T.W., 2012. Selenium as paleo-oceanographic proxy: A first assessment. Geochim. Cosmochim. Acta 89, 302–317.
Mitchell, K., Couture, R.-M., Johnson, T.M., Mason, P.R.D., Van Cappellen, P., 2013. Selenium sorption and isotope fractionation: Iron(III) oxides versus iron(II) sulfides. Chem. Geol. 342, 21–28.
Mitchell, K., Mansoor, S.Z., Mason, P.R.D., Johnson, T.M., Van Cappellen, P., 2016. Geological evolution of the marine selenium cycle: Insights from the bulk shale $\delta^{82/76}$Se record and isotope mass balance modeling. Earth Planet. Sci. Lett. 441, 178–187.
Nakada, R., Tanimizu, M., Takahashi, Y., 2013. Difference in the stable isotopic fractionations of Ce, Nd, and Sm during adsorption on iron and manganese oxides and its interpretation based on their local structures. Geochim. Cosmochim. Acta 121, 105–119.
Nielsen, S.G., Wasylenki, L.E., Rehkamper, M., Peacock, C.L., Xue, Z., Moon, E.M., 2013. Towards an understanding of thallium isotope fractionation during adsorption to manganese oxides. Geochim. Cosmochim. Acta 117, 252–265.
Ona-Nguema, G., Morin, G., Juillot, F., Calas, G., Brown Jr, G.E., 2005. EXAFS analysis of arsenite adsorption onto two-line ferrihydrite, hematite, goethite, and lepidocrocite. Environ. Sci. Technol. 39, 9147–9155.
Peak, D., Sparks, D.L., 2002. Mechanisms of selenate adsorption on iron oxides and hydroxides. Environ. Sci. Technol. 36, 1460–1466.
Perdew, J.P., Burke, K., Ernzerhof, M., 1996. Generalized Gradient Approximation Made Simple. Phys. Rev. Lett. 77, 3865–3868.
Pettine, M., Gennari, F., Campanella, L., 2013. The reaction of selenium(IV) with ascorbic acid: Its relevance in aqueous and soil systems. Chemosphere 90, 245–250.
Pinney, N., Kubicki, J.D., Middlemiss, D.S., Grey, C.P., Morgan, D., 2009. Density functional theory study of ferrihydrite and related Fe-oxyhydroxides. Chem. Mater. 21, 5727–5742.
Pogge von Strandmann, P.A.E., Stüeken, E.E., Elliott, T., Poulton, S.W., Dehler, C.M., Canfield, D.E., Catling, D.C., 2015. Selenium isotope evidence for progressive oxidation of the Neoproterozoic biosphere. Nat. Commun. 6, 1–10.
Pokrovsky, O.S., Galy, A., Schott, J., Pokrovski, G.S., Mantoura, S., 2014. Germanium isotope fractionation during Ge adsorption on goethite and its coprecipitation with Fe oxy(hydr)oxides. Geochim. Cosmochim. Acta 131, 138–149.
Qin, H.B., Zhu, J.M., Su, H., 2012. Selenium fractions in organic matter from Se-rich soils and weathered stone coal in selenosis areas of China. Chemosphere 86, 626–633.
Qin, H.B., Zhu, J.M., Liang, L., Wang, M.S., Su, H., 2013. The bioavailability of selenium and risk assessment for human selenium poisoning in high-Se areas, China. Environ. Int. 52, 66–74.
Qin, H.B., Takeichi, Y., Nitani, H., Terada, Y., Harada, T., Takahashi, Y., 2017a. Tellurium distribution and speciation in contaminated soils from abandoned mine tailings: Comparison with selenium. Environ. Sci. Technol. 51, 6027–6035.
Qin, H.B., Zhu, J.M., Lin, Z.Q., Xu, W.P., Tan, D.C., Zheng, L.R., Takahashi, Y., 2017b. Selenium speciation in seleniferous agricultural soils under different cropping systems using sequential extraction and X-ray absorption spectroscopy. Environ. Pollut. 225, 361–369.
Qin, H.B., Uesugi, S., Yang, S.T., Tanaka, M., Kashiwabara, T., Itai, T., Usui, A., Takahashi, Y., 2019. Enrichment mechanisms of antimony and arsenic in marine ferromanganese oxides: Insights from the structural similarity. Geochim. Cosmochim. Acta 257, 110–130.
Qin, H.B., Yang, S.T., Tanaka, M., Sanematsu, K., Arcilla, C., Takahashi, Y., 2021. Scandium immobilization by goethite: Surface adsorption versus structural incorporation. Geochim. Cosmochim. Acta 294, 255–272.
Rayman, M.P., 2008. Food-chain selenium and human health: emphasis on intake. Br. J. Nutr. 100, 254–268.
Rohrer, G.S., 2001. Structure and Bonding in Crystalline Materials. Cambridge University Press, pp. 14–17.
Rouxel, O., Ludden, J., Carignan, J., Marin, L., Fouquet, Y., 2002. Natural variations of Se isotopic composition determined by hydride generation multiple collector inductively coupled plasma mass spectrometry. Geochim. Cosmochim. Acta 66, 3191–3199.
Sassi, M., Chaka, A.M., Rosso, K.M., 2021. Ab initio thermodynamics reveals the nanocomposite structure of ferrihydrite. Commun. Chem. 4, 134.
Schauble, E.A., 2004. Applying stable isotope fractionation theory to new systems. Rev. Mineral. Geochem. 55, 65–111.
Schilling, K., Johnson, T.M., Dhillon, K.S., Mason, P.R.D., 2015. Fate of selenium in soils at a seleniferous site recorded by high precision Se isotope measurements. Environ. Sci. Technol. 49, 9690–9698.
Schilling, K., Basu, A., Wanner, C., Sanford, R.A., Pallud, C., Johnson, T.M., Mason, P.R.D., 2020. Mass-dependent selenium isotopic fractionation during microbial reduction of seleno-oxyanions by phylogenetically diverse bacteria. Geochim. Cosmochim. Acta 276, 274–288.
Schwertmann, U., Cornell, R.M., 2000. Iron Oxides in the Laboratory, second ed. Wiley-VCH.
Scott, M.J., Morgan, J.J., 1996. Reactions at oxide surfaces. 2. Oxidation of Se(IV) by synthetic birnessite. Environ. Sci. Technol. 30, 1990–1996.
Stüeken, E.E., 2017. Selenium isotopes as a biogeochemical proxy in deep time. Rev. Mineral. Geochem. 82, 657–682.
Stüeken, E.E., Foriel, J., Nelson, B.K., Buick, R., Catling, D.C., 2013. Selenium isotope analysis of organic-rich shales: advances in sample preparation and isobaric interference correction. J. Anal. At. Spectrom 28, 1734–1749.
Stüeken, E.E., Buick, R., Bekker, A., Catling, D., Foriel, J., Guy, B.M., Kah, L.C., Machel, H.G., Montañez, I.P., Poulton, S.W., 2015. The evolution of the global selenium cycle: Secular trends in Se isotopes and abundances. Geochim. Cosmochim. Acta 162, 109–125.
Takahashi, Y., Ariga, D., Fan, Q., Kashiwabara, T., 2015. Systematics of distributions of various elements between ferromanganese oxides and seawater from natural observation, thermodynamics, and structures. In: Subseafloor Biosphere Linked to Hydrothermal Systems: TAIGA Concept. Springer, pp. 39–48.
Takematsu, N., Sato, Y., Okabe, S., Usui, A., 1990. Uptake of selenium and other oxyanionic elements in marine ferromanganese concretions of different origins. Mar. Chem. 31, 271–283.
Tan, D., Zhu, J.M., Wang, X., Johnson, T.M., Li, S., Xu, W., 2020. Equilibrium fractionation and isotope exchange kinetics between aqueous Se(IV) and Se(VI). Geochim. Cosmochim. Acta 277, 21–36.
Tanaka, M., Ariga, D., Kashiwabara, T., Takahashi, Y., 2018. Adsorption mechanism of molybdenum(VI) on manganese oxides causing a large isotope fractionation. ACS Earth Space Chem. 2, 1187–1195.
Togo, A., Tanaka, I., 2015. First principles phonon calculations in materials science. Scr. Mater. 108, 1–5.
Urey, H.C., 1947. The thermodynamic properties of isotopic substances. J. Chem. Soc. 562–581.
Van Stempvoort, D.R., Reardon, E.J., Fritz, P., 1990. Fractionation of sulfur and oxygen isotopes in sulfate by soil sorption. Geochim. Cosmochim. Acta 54, 2817–2826.
Wang, W., Zhou, C., Liu, Y., Wu, Z., Huang, F., 2019. Equilibrium Mg isotope fractionation among aqueous Mg^{2+}, carbonates, brucite and lizardite: Insights from first-principles molecular dynamics simulations. Geochim. Cosmochim. Acta 250, 117–129.
Wasserman, N.L., Schilling, K., Johnson, T.M., Pallud, C., 2021. Selenium isotope shifts during the oxidation of selenide-bearing minerals. ACS Earth Space Chem. 5, 1140–1149.
Wasylenki, L.E., Rolfe, B.A., Weeks, C.L., Spiro, T.G., Anbar, A.D., 2008. Experimental investigation of the effects of temperature and ionic strength on Mo isotope fractionation during adsorption to manganese oxides. Geochim. Cosmochim. Acta 72, 5997–6005.
Wasylenki, L.E., Weeks, C.L., Bargar, J.R., Spiro, T.G., Hein, J.R., Anbar, A.D., 2011. The molecular mechanism of Mo isotope fractionation during adsorption to birnessite. Geochim. Cosmochim. Acta 75, 5019–5031.
Wasylenki, L.E., Schaefer, A.T., Chanda, P., Farmer, J.C., 2020. Differential behavior of tungsten stable isotopes during sorption to Fe versus Mn oxyhydroxides at low ionic strength. Chem. Geol. 558, 119836.
Wijnja, H., Schulthess, C.P., 2000. Vibrational spectroscopy study of selenate and sulfate adsorption mechanisms on Fe and Al (hydr)oxide surfaces. J. Colloid Interface Sci. 229, 286–297.
Xu, W.P., Zhu, J.M., Johnson, T.M., Wang, X.L., Lin, Z.Q., Tan, D.C., Qin, H.B., 2020. Selenium isotope fractionation during adsorption by Fe, Mn and Al oxides. Geochim. Cosmochim. Acta 272, 121–136.
Xu, W.P., Qin, H.B., Zhu, J.-M., Johnson, T.M., Tan, D.C., Liu, C.S., Takahashi, Y., 2021. Selenium isotope fractionation during adsorption onto montmorillonite and kaolinite. Appl. Clay Sci. 211, 106189.
Yang, S., Uesugi, S., Qin, H.B., Tanaka, M., Kurisu, M., Miyamoto, C., Kashiwabara, T., Usui, A., Takahashi, Y., 2018. Comparison of arsenate and molybdate speciation in hydrogenetic ferromanganese Nodules. ACS Earth Space Chem. 3, 29–38.
Yang, G.Q., Wang, S.Z., Zhou, R.H., Sun, S.Z., 1983. Endemic Se intoxication of humans in China. Am. J. Clin. Nutr. 37, 872–881.
Yuan, W., Saldi, G.D., Chen, J., Vetuschi Zuccolini, M., Birck, J.-L., Liu, Y., Schott, J., 2018. Gallium isotope fractionation during Ga adsorption on calcite and goethite. Geochim. Cosmochim. Acta 223, 350–363.
Zabinsky, S.I., Rehr, J.J., Ankudinov, A., Albers, R.C., Eller, M.J., 1995. Multiple-scattering calculations of X-ray-absorption spectra. Phys. Rev. B 52, 2995–3009.
Zhu, J.M., Wang, N., Li, S.H., Li, L., Su, H.C., 2008. Distribution and transport of selenium in Yutangba, China: impact of human activities. Sci. Total Environ. 392, 252–261.
Zhu, J.M., Johnson, T.M., Clark, S.K., Zhu, X.K., Wang, X.L., 2014. Selenium redox cycling during weathering of Se-rich shales: A selenium isotope study. Geochim. Cosmochim. Acta 126, 228–249.